Spatial proteomics reveals profound subcellular reorganization in human keratinocytes exposed to UVA light

Hellen P. Valerio[1]*, Felipe G. Ravagnani[1], Angela P. Y. Candela[1], Bruna D. C. da Costa[1], Graziella E. Ronsein[1]*, Paolo Di Mascio[1]*

[1] Department of Biochemistry, Institute of Chemistry, University of São Paulo, São Paulo, 05508-000, Brazil

*Correspondence: hellen.valerio@usp.br (Hellen P. Valerio), ronsein@iq.usp.br (Graziella E. Ronsein), pdmascio@usp.br (Paolo Di Mascio)

Summary

The effects of UV light on the skin have been extensively investigated. However, systematic information about how exposure to UVA light, the least energetic but the most abundant UV radiation reaching the Earth, shapes the subcellular organization of proteins is lacking. Using subcellular fractionation, mass-spectrometry-based proteomics, machine learning algorithms, immunofluorescence, and functional assays, we mapped the subcellular reorganization of the proteome of human keratinocytes in response to UVA light. Our workflow quantified and assigned subcellular localization and redistribution patterns for over 3000 proteins, of which about 600 were found to redistribute upon UVA exposure. Reorganization of the proteome affected modulators of signaling pathways, cellular metabolism and DNA damage response. Strikingly, mitochondria were identified as the main target of UVA-induced stress. Further investigation demonstrated that UVA induces mitochondrial fragmentation, up-regulates redox-responsive proteins and attenuates respiratory rates. These observations emphasize the role of this radiation as a potent metabolic stressor in the skin.

Introduction

Ultraviolet-A (UVA) light (315–400 nm) constitutes about 95% of all ultraviolet radiation (UVR) that reaches the Earth[1]. The causal association between UVR exposure and skin cancer is well established, but epidemiology has little capacity to distinguish between the carcinogenic effects of UVA and UVB[2]. At the molecular level, the effects of UVA and UVB in skin cells are of different natures, suggesting that each wavelength range defines a different path towards malignant transformation[3].

For example, UVB is absorbed by pyrimidines, giving rise to cyclobutane pyrimidine dimers (CPD) and pyrimidine (6-4) pyrimidone photoproducts. Thus, UVB's carcinogenic action depends on the direct generation of mutagenic DNA lesions[1]. On the other hand, UVA photons are poorly absorbed by the DNA, being more relevantly absorbed by other cellular chromophores[4]. In this sense, UVA relies on the generation of photoexcited species, such as singlet oxygen, that may lead to oxidative damage[5].

Skin cells orchestrate complex responses to light stress, coordinating gene expression, metabolism and protein function[6]. Protein function is fine-tuned in a sophisticated manner, involving modulations in abundance, chemical modifications, and spatial and temporal delimitations[7]. Mutational dynamics is the primary driver of carcinogenesis. However, modulation of metabolism and protein function can contribute to this process by impacting signaling, organelle interactions and cell fate decisions towards apoptosis, senescence or malignant transformation[2,8].

Even though the effects of UVR on DNA modification[9], gene expression[10], protein expression[11] and post-translational modifications[12,13] have been investigated, information about how specific UVR components shape the subcellular organization of proteins in cells is still lacking. Advances in high-throughput mass spectrometry[14,15] and microscopy[7,16] and machine learning applications for these techniques[17,18] allow proteome-wide investigations into subcellular localization dynamics and organellar communication in cells under stress. Spatial or organellar proteomics workflows may combine cell fractionation with mass spectrometry to characterize changes in protein levels in multiple subcellular niches[17]. Indeed, methods such as Protein Correlation Profiling (PCP)[19,20] and Hyperplexed Localisation of Organelle Proteins by Isotope Tagging (LOPIT)[21,22] and other organellar mapping approaches[23,24] have been developed to monitor protein dynamics over space in an unbiased manner.

The principle behind these methodologies is to quantify the distribution of proteins across subcellular fractions under different biological conditions. The fractionation profiles of proteins reflect the complexity of subcellular localization better than the presence or absence in a single purified fraction. Thus, they are used as an input for learning algorithms, allowing the prediction and classification of subcellular localization. Recently, machine learning pipelines predicted translocation events between subcellular niches by allowing the comparison of fractionation profiles under different biological conditions[25].

In light of these advances, we used spatial proteomics coupled with machine learning techniques to systematically analyze the subcellular reorganization of the proteome of skin cells in response to UVA radiation. Our results show that a low UVA dose, equivalent to about 20 minutes of midday sun exposure[26], leads to a profound spatial remodeling of the skin cells' proteome. We found that the spatial stress response relies on changes in mitochondrial dynamics, nucleocytoplasmic translocations triggered by DNA damage, and protein degradation. Furthermore, our results provide a resource for further investigations of UVA-triggered translocations.

Results

Workflow used to investigate proteome remodeling of skin cells under UVA light stress

An overview of the experimental protocol is shown in **Fig. 1A**. In the experimental pipeline, HaCaT skin cells were exposed to a non-cytotoxic low dose of UVA light (6 J/cm², using a simulator of the solar UVA spectrum) or kept in the dark under the same environmental conditions. Mock-treated and UVA-exposed cells were collected, the plasma membranes were lysed in hypoosmotic solution, and the organelles were separated by differential centrifugation. Fractions were collected after each centrifugation step, and proteins were quantified in each fraction by conventional label-free mass spectrometry. A total of 5351 protein groups were identified and quantified in 90 samples, comprising nine fractions for each of the five biological replicates of each condition. The dataset was filtered for proteins with label-free quantifications (LFQ) of greater than zero in at least one-third of all samples, yielding a matrix of 3287 protein groups. This step was performed to exclude proteins that were irregularly quantified across replicates and fractions.

Next, to assess if the dataset's structure reflected subcellular localization, we used three complementary approaches to inspect data quality, predict subcellular localization and infer protein translocation. First, we used t-SNE as a dimensionality reduction method overlaid with different databases (Uniprot, Gene Ontology and Cell Atlas) to inspect cluster formation. Second, we used a neural network algorithm to assess if subcellular localization could be predicted accurately by learning the fractionation patterns of organellar markers with well-established localization. Lastly, after validating the dataset's structure, we used the Translocation Analysis of Spatial Proteomics (TRANSPIRE) computational pipeline[25], which is based on a gaussian process classifier, to investigate changes in the subcellular landscape induced by UVA light in human keratinocytes. An overview of the computational workflow is presented in **Fig. 1B**. The results obtained by TRANSPIRE were further validated by conventional biochemical assays (**Fig. 1C**).

Validating the resolving power of the fractionation method

Following our workflow, we first inspected the t-SNE plot generated from the filtered dataset to reduce dimensionality and detect the presence of clusters. The plot revealed the presence of four main clusters in distinct regions (**Fig. 1S**). When overlaid with the subcellular localization data from three different databases (Uniprot, Cell Atlas and Gene Ontology), we found that the four clusters represented four distinct subcellular environments: the nucleus, cytosol, mitochondria, and secretory organelles. The database classifications were binned such that secretory organelles included proteins from the ER, peroxisome, Golgi, lysosome and plasma membrane (**Fig. 1S**).

Since this analysis showed that the fractionation scheme provides the resolution necessary for differentiating these four main subcellular compartments, we curated organellar markers for each compartment to investigate if protein localization could be predicted based on the fractionation scheme. The Uniprot and Gene Ontology classifications of subcellular localization were used for curating the organellar markers. Thus, for a protein to be considered an organellar marker, it had to be classified in both databases as uniquely pertaining to one subcellular niche among the four compartments (i.e., cytosol, nucleus, mitochondria and secretory) established through dimensionality reduction. The fractionation profiles of uniquely localized proteins were then manually inspected to assure that the markers were reproducibly quantified and did not present missing values across replicates in our experiment.

Based on these criteria, 247 organellar markers were curated into four subcellular niches: the cytosol (64), nucleus (75), mitochondria (60), and secretory organelles (48). Fractionation profiles of markers from different compartments present characteristic shapes, demonstrating that proteins from the same subcellular niche tend to fractionate similarly (profile plots, **Fig. 2A**). The t-SNE supports the patterns observed in the profile plots, showing that organellar markers from different compartments cluster in separate plot regions, while markers of the same compartment cluster similarly (**Fig. 2B**).

Following this analysis, a neural networks algorithm implemented in pRoloc[27], utilizing as references of each compartment the fractionation profiles of curated organellar markers, classified proteins into four discrete subcellular compartments. To assess the reproducibility of prediction across replicates, we applied the algorithm to each of the five biological replicates of each condition separately. **Fig. 2C** contains the t-SNE plots representing the most frequent classification of each protein across the five replicates for each condition. All of the 3287 protein groups were classified into four subcellular niches: the cytosol (623 ± 47 proteins, considering the mean and standard deviation across replicates), nucleus (640 ± 144), mitochondria (1293 ± 179), and secretory organelles (707 ± 183), with slight differences for the total number of classifications between conditions (**Fig. 2D**). The cellular compartment classification obtained for each replicate was then compared to the GO classification. The results revealed that the neural networks algorithm achieved a mean prediction accuracy of 75% in control samples and 73% in treated samples (**Fig. 2E**). Classifications were also highly reproducible, with 80 and 85% of all proteins in the treated and control samples, respectively, receiving the same classification in at least 3 out of 5 biological replicates (**Fig. 2F**). All classifications obtained from the machine learning algorithm are accompanied by classification probability scores that reflect the reliability of the assignment. In this context, low scores are often associated with profiles not directly modeled by the organellar markers used in the algorithm (e.g., multilocalized proteins)[24].

In addition, we analyzed if the dataset could provide sub-organellar resolution by overlaying the t-SNE plot with markers of sub-organellar compartments (obtained from Uniprot, Cell Atlas and Gene Ontology). The results indicate a partial divide between the mitochondrial matrix, membrane and nuclear subniches, such as the nucleolus,

nucleoplasm, and chromatin clusters (**Fig. 2G**). Moreover, the t-SNE plot also reveals that specific protein complexes colocalize *in vivo*. For example, our dataset's clustering of the heavy and light ribosome subunits and the proteasome supports the notion that the fractionation preserves the colocalization of interaction networks.

Altogether, these results indicate that the dataset is structured in a way that is dependent on subcellular localization, considering compartments delimited by membranes (i.e., organelles) and compartments delimited by protein complex formation (i.e., the nucleolus and the proteasome). This analysis provides a comprehensive investigation of HaCaT subcellular architecture, allowing for inferences about UVA-induced translocations.

UVA light elicits extensive changes in the subcellular distribution of proteins

Next, we used the recently developed TRASPIRE pipeline[25] to predict UVA-triggered translocation in the spatial proteomics dataset. This pipeline creates synthetic translocation classes from organellar markers, trains a Gaussian process classifier based on the synthetic translocation classes and predicts translocations in the actual dataset. The basis of this approach relies on first concatenating the organellar markers between the different biological conditions to produce synthetic markers. Then the synthetic markers are further clustered to provide different translocation and non-translocation classes, allowing the algorithm to predict the directionality of protein trafficking across subcellular niches.

The algorithm performs all possible combinations of organellar markers between conditions to generate synthetic translocations of different classes. In this sense, “Nucleus to Cytosol” and “Mitochondria to Mitochondria” would represent two different classes. Thus, the algorithm's output consists of the translocation classes attributed to each protein and translocation scores, calculated as described by Kennedy et al.[25]. False-positive rates (FPR) were calculated based on the learning model, and a 0.5% FPR threshold was applied to define a true translocation event.

Importantly, changes in the fractionation profile may reflect diverse phenomena, such as translocation events[23], altered organellar dynamics[24], or possibly altered rates of synthesis and degradation of proteins within specific subcellular niches[25]. Learning algorithms applied to spatial proteomics present limitations in differentiating among these events since they only classify proteins according to translocation classes[17,24].

As shown in **Fig. 3A**, the classifier achieved a high level of accuracy during training, reaching values above 90%, and identified 611 possible targets of translocation (FPR 0.5%) altogether. The number of proteins assigned to each translocation class is shown in **Fig 3B**. By aligning the translocation classes in a circular plot (**Fig. 3C**), it is possible to see that they are not equally distributed across the four subcellular niches. Indeed the efflux is more intense for secretory organelles than for other compartments. This observation possibly reflects the crucial role secretory organelles play in protein trafficking between different subcellular niches. Translocating proteins are significantly enriched for biological processes related to cellular localization ("cellular localization", "establishment of localization in cell', "cellular component organization") and mitochondrial translation ("mitochondrial translation elongation", "mitochondrial translation termination") (**Fig. 3D**). The GO terms for the cellular compartment indicate that translocating proteins are mainly cytosolic and mitochondrial, reinforcing the possible role of mitochondria in UVA-induced damage.

Further evaluation of the 12 highest scoring translocating proteins revealed that five (MAP2K3, PARP4, YTHDF2, OAS1, RNF114) were reported to be multilocalized according to the GO and Uniprot classifications (**Fig. 3E**). Previously, MAP2K3, RPS6KA4 and CLDN7 were reported to be UV-responsive[28–31]. Notably, MAP2K3, a protein responsible for activating the p38-MAPK signaling and one of the most significant pathways involved in the response against UV-induced stress in human cells, had the highest score[32].

Considering that mitochondrial translocation and nucleocytoplasmic translocations were some of the most frequent types of events predicted by the algorithm and are unequivocally relevant to UVA's biological action, we explored these processes in more depth, validating some translocation targets involved in the response of keratinocytes to DNA damage and UVA-induced metabolic stress.

Spatial remodeling provides clues about UVA's oxidative potential

We first focused on curating the translocation labels predicted by the algorithm using GO classifications and a review of the literature to validate specific UVA-triggered translocations between the cytoplasm and nucleus. The algorithm identified a total of 100 proteins that translocate between the cytosol and the nucleus, considering a 0.5% false-positive rate. The localization prediction of each protein in the control cells was

compared to the respective GO classification to achieve a more stringent list of translocation targets. We only kept proteins with concordant classifications for further analysis, which resulted in 67 out of the initial 100 proteins. Then, a literature review was performed to identify targets for which nucleocytoplasmic translocations had been previously identified, or at least for which dual nuclear-cytoplasmic localization and functions were previously reported. A total of 25 proteins fulfilled both conditions. These targets and their respective translocation scores are provided in the Supplementary Information.

The 25 protein targets play diverse biological roles. While some are transcription factors, others participate in nuclear cytoskeleton remodeling, signaling pathways and RNA processing. Nucleocytoplasmic translocations induced by DNA damage have been previously reported for UBL4A[33], CETN2[34,35], FAF1[36], CTBP1[37], RELA[38], NFKB1[38], CIAO2B[39] and CSNK2[40]. Moreover, three proteins (CIAO2B[39], CETN2[34] and CSNK2[41]) have been shown to interact with nucleotide-excision repair (NER) components, which are involved in recognizing and repairing cyclobutane pyrimidine dimers (CPD) generated as a consequence of UVR exposure.

The β subunit of CSNK2 (CSNK2B), one of the strongest hits, was first implicated in the DNA damage response through its interaction with the tumor suppressor p53[40]. CSNK2 is also involved in the phosphorylation of two NER components (XPB, CETN2)[42,43]. Additionally, it has been demonstrated that XPC- and XPD-deficient cells expressing higher levels of CSNK2B are more resistant to UV-induced death[44], especially since increases in CSNK2B lead to dramatic increases in CSNK2 activity[45]. In our experiment, CSNK2B shifts from a central position in the cytosolic cluster in controls to the interface between the cytosolic and nuclear clusters in irradiated samples (**Fig. 4A**). This behavior is consistent with a significant difference between groups observed for this protein in the profile plot, especially in the last fraction that is enriched with cytosolic proteins (**Fig. 4B**). Redistribution of CSNK2B from the cytoplasm to the nucleus upon irradiation was corroborated by immunofluorescence, indicating that UVA exposure leads to the translocation of cytosolic CSNK2B to the nucleus (**Fig. 4C**).

To confirm that our irradiation conditions generated significant levels of DNA damage, we performed a modified version of the comet assay to detect different types of DNA lesions in cells following exposure to 6 J/cm² of UVA light (**Fig. 4D**). The comet assay was modified through the addition of formamidopyrimidine-DNA glycosylase (FPG),

endonuclease V (endoV) and endonuclease III (endoIII) to detect oxidized pyrimidines, CPD and oxidized purines, respectively. The predominant types of lesions generated immediately after exposure to UVA are CPD and oxidized purines, in agreement with what has been previously described for this radiation dose[46]. However, while oxidized purines seem to be efficiently removed from the DNA one hour after exposure to the radiation, CPD reaches a plateau and persists in HaCaT cells for at least four hours after irradiation. The DNA lesion profile identified here and its repair kinetics are consistent with NER activation, consequently triggering translocation events associated with this pathway. Even though UVA generates lower levels of CPD than UVB, CPD generation can still promote CSNK2B recruitment to the nucleus.

The algorithm also predicted the translocation of two NF-κB subunits (RELA and NFKB1). The RELA subunit contains the transactivation domain, responsible for the transcription factor function[38], and we chose this subunit for further validation by confocal microscopy. In our translocation experiment, RELA of non-irradiated samples presents a typical cytosolic fractionation pattern, with peaks in the 6th and last fractions. However, upon irradiation, we observe a decrease in abundance in the 6th fraction and an increase in the 3rd fraction (**Fig. 5A**). Changes between conditions can also be observed in the t-SNE plots (**Fig. 5B**). Importantly, RELA is in the center of the cytoplasmic cluster in the control samples but shifts to the interface between the cytoplasmic and nuclear clusters following irradiation. To investigate NF-κB dynamics further, we immunolabeled the RELA subunit and performed immunofluorescence (IF) microscopy. Immunolabeling of the RELA subunit revealed a reduction in the overall levels of this transcription factor (**Fig. 5C**), which seems to be consistent with the attenuated abundance observed in the 6th fraction of irradiated cells. In control cells, RELA is present throughout the entire cytoplasm. However, in irradiated cells, RELA labeling weakens, assuming punctate structures and possibly reflecting the cellular compartmentalization of protein degradation. Previous studies addressing functional aspects of NF-κB in HaCaT cells exposed to UVA light revealed contradictory roles for this protein in this type of stress response[47–49]. It was reported that UVA doses lower than 1 J/cm² induce NF-κB activation, while higher doses lead to decreased NF-κB levels[50]. Moreover, in agreement with our results, UVA light has been previously described to induce NF-κB degradation in human keratinocytes[47]. In this context, deuterated water enhanced UVA-induced NF-κB degradation and low concentrations of

sodium azide abolished this effect. Importantly, since deuterated water prolongs the half-life of singlet oxygen and sodium azide is a singlet oxygen quencher, UVA-induced NF-κB degradation has been mainly attributed to singlet oxygen generation.

UVA light promotes metabolic stress through mitochondrial fragmentation

Since mitochondrial proteins have been detected as the significant pool of translocating targets, we investigated and validated the role of the spatial reorganization of mitochondrial components in the response against UVA-induced stress. Interestingly, most of the mitochondrial proteins classified as translocating are structural and uniquely localized to the mitochondria. These proteins are not usually involved in translocations across different subcellular niches. Examples include mitoribosomal subunits and electron transport chain components (**Fig. 6A**). We hypothesized that alterations in the fractionation profiling of these proteins between conditions might represent alterations in mitochondrial morphology and not necessarily translocations. Thus, we immunolabeled a respiratory chain component (COX4I1) and performed an IF experiment. As shown in **Fig. 6B**, in controls, COX4I1 displays the typical tubular appearance of the mitochondrial network and forms punctate structures in irradiated samples, a sign of UVA-induced mitochondrial fragmentation.

Besides detecting changes in the fractionation profile of structural mitochondrial proteins, our algorithm also detected the movement of some proteins that have been previously described as migrating from the mitochondria to the nucleus. Thus, to determine if changes in the fractionation profiling of non-structural mitochondrial proteins predicted as translocations also reflect mitochondria fragmentation, we validated the spatial redistribution of fumarase (FH) and ornithine aminotransferase (OAT) in irradiated cells. Notably, both FH and OAT have been reported to translocate from the mitochondria to the nucleus[51,52]. We also monitored PDHA1 in the same experiment to check for colocalization of structural and non-structural mitochondrial proteins. The results showed that both FH and OAT display similar migration patterns in the t-SNE, shifting from the interface between the mitochondrial and nuclear clusters in control cells to the interface between the mitochondrial and cytosolic clusters in treated cells (**Fig. 7A-B**). Thus, both proteins display decreasing levels in the first fractions (1-3) of irradiated samples compared to control samples, accompanied by increased levels in the last fraction (**Fig. 7C-D**)**.** Immunofluorescence images confirmed the same mitochondrial fragmentation phenomenon observed for labeling structural

mitochondrial proteins (COX4I1 and PDHA1), reinforcing our previous results (**Fig. 7E-F**).

Since cells displaying fragmented mitochondria usually have a reduced respiratory capacity[53], we measured oxygen consumption rates in HaCaT cells exposed to UVA light using a Seahorse Analyzer XF24 to validate the functional impact of mitochondrial fragmentation. Accordingly, basal and maximal mitochondrial respiration are decreased in irradiated cells compared to control samples, supporting the notion of electron transport chain dysfunction (**Fig. 8A**). Changes in mitochondrial respiration were accompanied by a decrease in the cell's reductive power up to 24 hours after irradiation, without losses in viability, as inferred by the MTT results and the trypan blue exclusion assay (**Fig. 2S**). The reduction in the cell's reductive power occurs in a radiation dose-dependent manner. Importantly, we did not observe leakage of cytochrome *c* from the mitochondria to the cytosol or BAX translocation, as would be expected of cells entering apoptosis (**Fig. 2S**). We also searched for changes in the fractionation profiles of MFN1 and MFN2, two key regulators of mitochondrial dynamics, to further confirm mitochondrial fragmentation. Indeed, as shown in **Fig. 8B**, both proteins displayed differential fractionation profiles between biological conditions.

Since UVA light is known to cause oxidative and genotoxic stresses[1] and help explain the changes in mitochondrial dynamics, we tested if a low dose of UVA could promote alterations in the levels of stress-responsive proteins one and a half hours after radiation exposure. After this period, 138 proteins were significantly modulated between groups (**Fig. 8C**). Focusing on stress-responsive proteins (**Fig. 8C**), we observed the up-regulation of DNA damage response components (RAD23B and XRCC6), a few DNA replication licensing factors, antioxidant enzymes (GSTP1 and PRDX1) and heat shock proteins. Additionally, a few subunits of the electron transport chain complexes and a few redox-responsive proteins (CAT and PRDX3) were down-regulated.

By analyzing the fold change of proteins between treatments in a compartment-specific fashion (**Fig. 8D**), we found that the fold change of mitochondrial proteins is significantly lower when compared to the whole proteome ($p = 1.47 \times 10^{-17}$, Wilcox test, FDR correction), suggesting that decreasing levels of electron transport chain components recapitulate mitochondrial proteome changes as a whole. Importantly, mitochondrial fragmentation usually facilitates mitophagy of damaged mitochondria[54].

These results show that exposing skin cells to UVA light impacts mitochondrial dynamics, leading to fragmentation, respiratory dysfunction, and the upregulation of stress response proteins.

Discussion

The present study is the first to provide a map of subcellular protein reorganization induced by the UVA component of sunlight in a skin cell type. High sensitivity MS-based proteomics coupled to machine learning algorithms quantified and assigned subcellular localization and redistribution patterns for over 3000 proteins in human keratinocytes exposed to UVA light. Our unbiased approach revealed that a single low dose of UVA light could affect the proteomic architecture of skin cells, provoking the reorganization of subcellular structures due to genotoxic and metabolic stresses.

In this work, about 20% of the identified and quantified proteins (over 600 proteins from a total of 3200) relocalized in response to UVA exposure. Our results showed that redistribution of proteins across subcellular niches encompass different phenomena, such as changes in organelle dynamics, translocation and targeting for degradation. After considering all redistribution events, important modulators of cellular metabolism, mitochondrial function, protein and vesicle trafficking, signaling pathways and DNA damage recognition and repair were identified.

Previously it was reported that DNA damage response rewires metabolic circuits, fine-tuning protein synthesis, trafficking and secretion[55]. However, it is not clear how genotoxic components of the sunlight affect protein localization or organelle architecture and interactions. We showed that UVA exposure caused nucleocytoplasmic translocations induced by DNA damage. For instance, our algorithm detected with high confidence the nucleocytoplasmic translocation of CSNK2B in UVA-irradiated cells, a finding further confirmed by confocal microscopy. CSNK2 has many biological targets, maintaining cellular viability and the DNA damage response[41,56,57]. Its role in the cellular response against UVR has been described in terms of its interaction with p53 and NER components[41]. Indeed, using the Comet assay, we observed that UVA radiation leads to simultaneous CPD formation and CSNK2B translocation. We also monitored DNA damage over time and observed that CPDs are repaired over 24 hours, indicating NER activation. Collectively, these results demonstrate that UVA triggers a

classical DNA damage signaling pathway, even though it generates lower levels of CPD than the more energetic UVB light.

Besides having oxidative effects on the DNA, we also provide evidence that UVA can target NF-κB's catalytic subunit for degradation, which likely occurs in a singlet oxygen-dependent manner, as previously proposed[47]. Since NF-κB is ubiquitously distributed across the cytoplasm, the extensive degradation of this protein indicates that the oxidative potential of UVA may bear consequences for the entire surface of cells. Importantly, this evidence also reinforces the differential immunomodulatory effects of UVA and UVB on the skin[26] since UVB has been extensively reported to trigger NF-κB's nuclear translocation and subsequent activation of this transcription factor[58]. In contrast, UVA seems to trigger the opposite effect.

The most striking result of our systematic proteomic profiling was identifying mitochondria as the main target of UVA-induced stress. We showed that UVA induces mitochondrial fragmentation, up-regulates redox-responsive proteins and reduces the respiratory rate, leading to changes in the cells' overall energetic status. These results expand on previous characterizations of mitochondrial dysfunction in response to UV radiation[59,60] and show that alterations occur even with acute low-dose exposures to UVA, the least energetic component of the UV spectrum. It has been suggested that UVA-induced deletions in mtDNA underlie the long-term effects of UVA during photoaging[61]. However, our results suggest that UVA also has short-term effects on the mitochondria, acting as a potent stressor immediately after exposure. Some endogenous metabolites have been proposed to play a role in UVA's photosensitization in skin cells, such as flavin-derivatives, NADH, NADPH, FADH, urocanic acid, porphyrins and some sterols[5]. Mitochondria, in particular, contain high concentrations of putative UVA chromophores, such as flavin-derivatives, NADH, FADH and NADPH, which could mediate the damage to this organelle.

Several studies showed that high doses of UVB irradiation (e.g., > 100 mJ/cm²) trigger mitochondrial fragmentation in keratinocytes[60,62,63]. On the other hand, UVC (60 mJ/cm²) leads to mitochondrial hyperfusion instead of fragmentation in mouse fibroblasts, suggesting that UVR-induced modulations of mitochondrial dynamics are complex and context-dependent[64]. Our results show that even low doses of less energetic UVA light induce mitochondrial fragmentation.

UVB-induced mitochondrial fragmentation is dependent on DRP1 mitochondrial translocation, with partial roles for MFN1 and OPA1[60], frequently followed by apoptosis[62,63]. In our experiments with UVA irradiation, we did not detect changes in molecular markers of apoptosis, such as cytochrome *c* leakage from mitochondria, BAX translocation, or attenuated cell viability. Moreover, we did not observe changes in the abundance or subcellular reorganization of DRP1 or OPA1. However, we did observe that MFN1 and MFN2 displayed a differential fractionation profile between conditions, suggesting that UVA may affect their function differently than other UV wavelength ranges. Importantly, MFN1 and MFN2 modulations have been reported to occur in response to oxidative stress [65]. For example, fibroblasts exposed to exogenous H_2O_2 up-regulate the ubiquitination of MFN1 and MFN2, triggering mitochondrial fragmentation[66].

Our study has several strengths. First, machine learning predictions involving DNA damage response, inflammation and cellular metabolism were validated using confocal microscopy and functional assays. Second, our dataset opens up possibilities for further investigation of UVA-triggered translocation events in less studied subcellular niches. Furthermore, ER and Golgi vesiculation occur in UV-exposed cells[55], and our data suggest that proteins from these compartments are redistributed upon stress.

Our work also has some limitations. Machine learning algorithms applied to spatial proteomics are not developed to differentiate between protein translocation events, altered organellar dynamics, or altered protein synthesis and degradation rates within specific subcellular niches. However, our biochemical validations unequivocally differentiated among these events.

In summary, our dataset provides valuable information about UVA-triggered translocation events in subcellular niches. Our experimental strategy employing cellular fractionation, MS-based proteomics and machine learning algorithms revealed UVA redistributed approximately 20% of the skin cell proteome, highlighted by the up-regulation of redox-responsive proteins, DNA damage and mitochondrial fragmentation.

Materials and Methods

Cell Culture

HaCaT cell line, a spontaneously immortalized human keratinocyte, was cultured in 5% CO_2 at 37°C and grown in Dulbecco's Modified Eagle's Medium (DMEM) supplemented with 10% fetal bovine serum, 100 U/mL penicillin and 100 ug/mL streptomycin. Professor Mauricio S. Baptista (Institute of Chemistry, University of São Paulo) provided the cell line, and it was tested for mycoplasma contamination.

Irradiation conditions

An Oriel SOL-UV 2 solar simulator (Newport, USA) equipped with a Xenon arc lamp was used for cell irradiation. The simulator was equipped with an IR bandpass blocking filter plus a UVB-blocking filter (emission spectra of the simulator radiation with and without the UVB-blocking filter are displayed in **Fig. 2S**). Before irradiation, the simulator's output was measured with a dosimeter from International Light Inc (Newburyport, MA, USA), model IL1700, with a SED033 detector. Using the IR and UVB blocking filters, the output measured in the area where the cell plates would be positioned, at a 10 cm distance from the light source, yielded a mean of 5.0 mW/cm², with a maximum variation of 10% between biological replicates. Each dish was irradiated for 26 minutes, corresponding to a total dose of 6 J/cm², which humans can be exposed to during routine daily living without affecting cellular viability (**Fig. 2S**). Cells were washed three times with phosphate-buffered saline (PBS) and kept in PBS during irradiation (26 minutes). Mock-treated controls were kept in PBS and maintained in the dark at room temperature for the same amount of time.

Subcellular proteome sample preparation

For the spatial proteomics assay, two million cells were plated in 100 mm dishes 48 hours before the experiments (until cells reached 80-90% confluency). An entire dish containing around eight million cells yielded at least 10 µg of protein in the fraction with the lowest yield, which was enough for mass spectrometry analysis.

Cells were trypsinized and harvested by centrifugation 30 minutes after irradiation. The cell pellet was washed twice in PBS and incubated for 10 minutes in 1 mL of hypotonic lysis buffer (25 mM Tris-HCl, pH 7.5, 50 mM Sucrose, 0.5 mM $MgCl_2$, 0.2 mM EGTA) on ice. Cells were then transferred to a Potter-Elvehjem homogenizer and

homogenized with 30 strokes on ice (until at least 70% of cells were stained with trypan blue). After homogenization, 110 µL of hypertonic sucrose buffer (2.5 M sucrose, 25 mM Tris pH 7.5, 0.5 mM $MgCl_2$, 0.2 mM EGTA) was used to restore osmolarity. The cell lysate was transferred to 2 mL tubes and centrifuged twice at 200 × *g* for 5 minutes to remove intact cells. The lysate was then subjected to a series of differential centrifugations: 1000 × *g* for 10 minutes, 3000 × *g* for 10 minutes, 5000 × *g* for 10 minutes, 9000 × *g* for 15 minutes, 12000 × *g* for 15 minutes, 15000 × *g* for 15 minutes, 30000 × *g* for 20 minutes and 80000 × *g* for 40 minutes. In total, each of the five biological replicates of each condition yielded nine fractions. The supernatant was collected because it contains the remaining cytosolic proteins. Afterward, fractions enriched with different organelles were lysed in 8 M urea containing 0.1% deoxycholate. The total protein concentrations were quantified using a BCA assay kit (Thermo Scientific), and 10 µg of protein per fraction were digested and analyzed by mass spectrometry.

Protein digestion

Aliquots corresponding to 10 µg of protein per sample were reduced with 5 mM dithiothreitol for one hour, alkylated with 15 mM iodoacetamide for 30 minutes, diluted ten-fold with 100 mM ammonium bicarbonate, and digested by the addition of two aliquots of trypsin (1:40 and 1:50, respectively, with an interval of four hours between the additions). The samples were digested overnight at 30°C with agitation (400 rpm). Digestion was stopped by adding 4% trifluoracetic acid (TFA), and then the samples were dried. Samples were desalted using the StageTip protocol [67]. Peptides were washed ten times with 0.1% TFA in the StageTips and eluted with 50% acetonitrile and 0.1% TFA.

LC-MS/MS measurements

Each sample was injected in an Orbitrap Fusion Lumos mass spectrometer (Thermo Fisher Scientific, Bremen, Germany) coupled to a Nano EASY-nLC 1200 (Thermo Fisher Scientific, Bremen, Germany). Peptides were injected into a trap column (nanoViper C18, 3 µm, 75 µm × 2 cm, Thermo Scientific) with 12 µL of solvent A (0.1% formic acid) at 980 bar. After this period, the trapped peptides were eluted onto a C18 column (nanoViper C18, 2 µm, 75 µm × 15 cm, Thermo Scientific) at a flow rate of 300 nL/min and subsequently separated with a 5-28% acetonitrile gradient with 0.1%

formic acid for 80 minutes, followed by a 28-40% acetonitrile gradient with 0.1% formic acid for 10 minutes.

The eluted peptides were detected in the data-dependent acquisition mode under positive electrospray ionization conditions. A full scan (*m/z* 400-1600) was acquired at a 60000 resolution, followed by HCD fragmentation of the most intense ions, considering an intensity threshold of 5×10^4. Ions were filtered for fragmentation by the quadrupole with a transmission window of 1.2 *m/z*. HCD fragmentation was performed with a normalized collision energy of 30, and the Orbitrap detector analyzed the fragments with a 30000 resolution. The number of MS2 events between full scans was determined by a cycle time of 3 seconds. A total of 5×10^5 and 5×10^4 ions were injected in the Orbitrap with accumulation times of 50 and 54 seconds for the full scan and MS2 acquisition, respectively. Monocharged ions or ions with undetermined charges were not selected for fragmentation.

Comet assay

A total of 500,000 cells were plated in 6-well plates 24 hours before the experiment (n = 3). After irradiation, cells were trypsinized and collected by centrifugation. The supernatant was discarded, and cell pellets were mixed with 100 µL of PBS. 10 µL of cell suspension was added to 90 µL of 0.5% low melting point agarose. Subsequently, 75 µL of this cell suspension was pipetted onto slides pre-coated with 1.5% normal melting point agarose. Slides were covered with coverslips and kept at 4°C for 30 minutes to allow the agarose to solidify. Next, the coverslips were removed, and the slides were kept in a tank containing lysis buffer (2.5 M NaCl, 100 mM EDTA, 10 mM Tris, 1% Triton X-100, and 10% DMSO, pH 10) overnight at 4°C in the dark.

After lysis, slides were washed with cold PBS three times in the dark and immersed three times in cold reaction buffer (40 mM HEPES, 0.1 M KCl, 0.5 mM EDTA, 0.2 mg/mL BSA, pH 8) for 5 minutes each time. After that, the reaction buffer or reaction buffer containing T4 endonuclease V (0.1 U/mL), FPG (0.2 U/mL) or endonuclease III (10 U/mL) enzymes were pipetted onto each slide. Coverslips were placed over the slides, and they were incubated for 30 minutes at 37°C in the dark. The slides were then transferred to cold electrophoresis buffer (10 M NaOH, 200 mM EDTA, pH 13 in water) and incubated for 20 minutes. Then, the slides were submitted to electrophoresis for 20 minutes at 25 V, 300 mA. After electrophoresis, the slides were immersed in

neutralizing solution (0.4 Tris, pH 7.5) three times for 5 minutes each time and fixed in methanol for 10 minutes. After washing, all the slides were air-dried at room temperature. The DNA was stained with 20 µL of a solution containing 2.5 ug/mL of propidium iodide for 10 minutes. Fifty randomly selected comets per sample were analyzed on a fluorescence microscope (Olympus BX51) using the Komet 6 software. Two technical and four biological replicates were analyzed per condition.

Immunofluorescence

Cells were seeded on 8-well Lab-Tek® II Chambered Coverglass plates (Thermo Scientific, # 155409) under standard cell culture conditions. Samples were fixed with ice-cold 4% paraformaldehyde in PBS without Ca^{2+} and Mg^{2+}. After removing the PFA, the cells were incubated for 20 minutes at room temperature with freshly prepared permeabilization buffer (0.1 % Triton X-100, PBS, pH 7.4). After that, cells were washed in PBS three times for 5 minutes each time.

For cell staining, samples were first rinsed for one hour with blocking buffer (3% fetal bovine serum, PBS, pH 7.4) at room temperature. Then, primary antibodies (OAT, Invitrogen #PA5-66715, 1:500; Fumarase, Invitrogen #PA5-82899, 1:500; Casein Kinase 2 beta, Abcam #ab151784, 1:500; PDHA1 [9H9AF5], Abcam #ab110330, 1:200, and COX4I1 Abcam #ab33985) were diluted (as indicated above) in blocking buffer and incubated overnight at 4°C. Next, the chambered coverglass plates were rinsed three times with PBS and cells were labeled with fluorescently conjugated secondary antibody (anti-Rabbit Alexa Fluor 488, Invitrogen #A-11008, 1:500; anti-Mouse Alexa Fluor 647, Abcam # ab150119, 1:500) in blocking buffer for one hour at room temperature. Afterward, unbound secondary antibodies were removed by washing with PBS three times for 5 minutes each at room temperature. Finally, nuclei were labeled with 1 µg/mL Hoechst 33342 in PBS (Invitrogen #H1399). Imaging was performed in PBS. A Zeiss LSM 710 laser scanning confocal microscope was used, and cells were imaged using x63 oil immersion objective (Plan Apochromat NA 1.40).

Respirometry

One day before the experiment, on four different days, 60,000 cells were plated on XF24 cell plates (Agilent) to measure cell respiration. After irradiation, PBS was replaced by DMEM without sodium bicarbonate, and cells were incubated for 1 hour at

37°C and atmospheric pressure of CO_2. Oxygen consumption rate (OCR) was measured in a Seahorse XF24 Analyzer (Agilent), before and after subsequent additions of 1 µM oligomycin, 1 µM CCCP and a mix of 1 µM antimycin and 1 µM rotenone. Each compound was added after three cycles of measurements of 3 minutes each. The concentration of CCCP was determined through the previous titration. At the end of the experiments, each well was washed once with PBS and proteins were resuspended in 100 µM ammonium bicarbonate, containing 8 M urea and 1% sodium deoxycholate. After homogenization, protein concentration was determined by using a BCA assay kit. The OCR values were normalized by the amount of total protein in each well.

Statistical Analysis

Descriptive data analysis

Raw files were processed using MaxQuant[68]. Each fraction was considered a different sample in the experimental design annotation file required for the MaxQuant analysis. A matrix of relative quantification data (LFQ)[69] for proteins in each fraction was obtained and used for subsequent analysis. Each protein was normalized by the total sum of the LFQs for a given replicate/cell map, yielding a value between 0 and 1. Proteins that were not quantified in at least 30 of the 90 samples were filtered out to remove uninformative fractionation profiles with missing values generated by stochastic fragmentation in the shotgun proteomics approach.

Dimensionality reduction was achieved using the t-distributed stochastic neighbor embedding technique (t-SNE)[70]. The fractionation data was plotted with different perplexity parameters (perplexity = 30 yielded the best cluster separation). The plots were overlaid with categorical subcellular classifications from the Cell Atlas initiative[71], Uniprot[72] and Gene Ontology[73] databases, providing information on the clusterization of different subcellular compartments.

Organellar markers were selected based on a previous subcellular proteomics study[22] and the curation of proteins classified as unimodally distributed by the Cell Atlas, Uniprot and Gene Ontology databases. Markers had to be reproducible across all replicates, and profile plots were manually curated to remove proteins with missing values. Organellar markers from four different compartments (cytosol, mitochondria, nucleus, and secretory organelles) were assigned with different colors to visualize

598 clusterization in the t-SNE plots. The secretory compartment comprises proteins
599 initially assigned to peroxisomes, endoplasmic reticulum (ER), plasma membrane,
600 Golgi apparatus and lysosomes. These organelles were grouped under the term
601 "secretory" because they share similar fractionation profiles that were not well
602 distinguished by the machine learning algorithms.

603 **Localization prediction**

604 As described previously[27,74], a supervised machine learning approach was used for the
605 subcellular localization prediction. We used a model of an averaged neural networks
606 algorithm[27] to produce the paper's results, but a support vector machine was also tested
607 and yielded similar results. The organellar markers were used to train the model for
608 subcellular localization prediction. Organellar markers were divided into a training and
609 validation set (80/20% proportion for each set) with a 5-fold cross-validation through
610 100 iterations of the algorithm. We used a grid search to achieve hyperparameter tuning.
611 The accuracy of the classifier was estimated through the F1 score[74], and the best
612 hyperparameters were chosen according to the accuracy of the classifier. The best
613 network size ranged from 4 to 6, and the best decay was 10^{-4}.

614 **Translocation prediction**

615 The TRANSPIRE pipeline was used for the translocation prediction, as previously [25].
616 Curated organellar markers were utilized to generate synthetic translocations, which are
617 then used to train the learning algorithm in distinguishing translocation classes and
618 consequently translocating from non-translocating proteins. In brief, each organellar
619 marker in the control samples is concatenated with every other organellar marker of the
620 treated samples, producing synthetic translocations and non-translocations (when
621 markers of the same compartment are concatenated). For example, a synthetic
622 translocation that simulates the migration of a protein from the nucleus to the cytosol
623 would have a fractionation profile that is characterized by the combination of a nuclear
624 marker profile in all control samples (45 fractions) with the cytosolic marker profile in
625 the treated samples (also 45 fractions, yielding a total of 90 "fractions" per synthetic
626 translocation).

627 Synthetic translocations were used to train a Stochastic Variational Gaussian Process
628 Classifier (SVGPC) implemented in TRANSPIRE through the GPFlow package (built
629 upon the TensorFlow platform in Python). This model is composed of a kernel function,

a likelihood function, n latent variables (which account for the number of translocation classes), a training set, and a subset of the training set used as inducing points[25]. The model implemented in TRANSPIRE uses softmax as a likelihood function to improve score calibration.

Hyperparameter tuning involved choosing the kernel type (squared exponential, rational quadratic, exponential Matern32 and Matern52, as implemented by TRANSPIRE through GPFlow) and the number of inducing points (ranging from 1 to 500). The synthetic translocation data were divided into training, validation, and test sets in a 50/20/20% proportion, respectively, during training. The training data was further split into five balanced folds during hyperparameter tuning, allowing for a 5-fold cross-validation. A class imbalance was prevented by allowing the most frequent translocation classes to have, at most, three times more proteins than the least frequent. The best hyperparameters selected through the grid search were the squared exponential kernel and 30 inducing points (optimization plots are shown in the Supporting Information). The results were evaluated by maximizing the evidence lower bound (ELBO) using the Adam optimizer. Afterward, the resulting model was used to predict translocations in the actual dataset and performance was evaluated based on the held-out test partition of the synthetic translocation data.

The output of the TRANSPIRE pipeline entails the classification of a translocation class (e.g., “Nucleus to Cytosol”) for each protein plus a classifier score. The classifier score ranges from 0 to 1 for each translocation class, and the sum of the scores for all classes for each protein should be equal to 1. Class prediction is based on the highest classifier score for a given translocation class. This score is referred to as “predicted scores” in the spreadsheets in the Supporting Information. Additionally, the TRANSPIRE pipeline provides a translocation score, defined as the sum of the predicted scores for all true translocation classes. This score accounts for situations in which high classifier scores are split among at least two translocation classes.

TRANSPIRE also allows for the computation of false-positive rates (FPR), based on the model’s performance, setting thresholds for the translocation scores to minimize the likelihood of false positives. Herein, we adopted a 0.5% FPR to generate a more stringent list of translocation targets.

References

1. Schuch, A. P., Moreno, N. C., Schuch, N. J., Menck, C. F. M. & Garcia, C. C. M. Sunlight damage to cellular DNA: Focus on oxidatively generated lesions. *Free Radic. Biol. Med.* **107**, 110–124 (2017).
2. El Ghissassi, F. *et al.* A review of human carcinogens--part D: radiation. *Lancet Oncol.* **10**, 751–752 (2009).
3. Premi, S. *et al.* Chemiexcitation of melanin derivatives induces DNA photoproducts long after UV exposure. *Science* **347**, 842–847 (2015).
4. Ikehata, H. Mechanistic considerations on the wavelength-dependent variations of UVR genotoxicity and mutagenesis in skin: The discrimination of UVA-signature from UV-signature mutation. *Photochem Photobiol Sci* **17**, 1861–1871 (2018).
5. Wondrak, G. T., Jacobson, M. K. & Jacobson, E. L. Endogenous UVA-photosensitizers: mediators of skin photodamage and novel targets for skin photoprotection. *Photochem. Photobiol. Sci.* **5**, 215–237 (2006).
6. Chen, H., Weng, Q. Y. & Fisher, D. E. UV Signaling Pathways within the Skin. *J Invest Dermatol* **134**, 2080–2085 (2014).
7. Thul, P. J. *et al.* A subcellular map of the human proteome. *Science* **356**, (2017).
8. de Gruijl, F. R., van Kranen, H. J. & Mullenders, L. H. F. UV-induced DNA damage, repair, mutations and oncogenic pathways in skin cancer. *Journal of Photochemistry and Photobiology B: Biology* **63**, 19–27 (2001).
9. Moreno, N. C. *et al.* Whole-exome sequencing reveals the impact of UVA light mutagenesis in xeroderma pigmentosum variant human cells. *Nucleic Acids Research* **48**, 1941–1953 (2020).
10. He, Y.-Y. *et al.* Expression Profiling of Human Keratinocyte Response to Ultraviolet A: Implications in Apoptosis. *Journal of Investigative Dermatology* **122**, 533–543 (2004).
11. Edifizi, D. *et al.* Multilayered Reprogramming in Response to Persistent DNA Damage in C. elegans. *Cell Reports* **20**, 2026–2043 (2017).
12. Elia, A. E. H. *et al.* Quantitative Proteomic Atlas of Ubiquitination and Acetylation in the DNA Damage Response. *Mol. Cell* **59**, 867–881 (2015).
13. Zhou, C. *et al.* Profiling DNA damage-induced phosphorylation in budding yeast reveals diverse signaling networks. *Proc Natl Acad Sci USA* **113**, E3667–E3675 (2016).
14. Larance, M. & Lamond, A. I. Multidimensional proteomics for cell biology. *Nature Reviews Molecular Cell Biology* **16**, 269–280 (2015).
15. Breker, M. & Schuldiner, M. The emergence of proteome-wide technologies: systematic analysis of proteins comes of age. *Nature Reviews Molecular Cell Biology* **15**, 453–464 (2014).
16. Mattiazzi Usaj, M. *et al.* High-Content Screening for Quantitative Cell Biology. *Trends Cell Biol.* **26**, 598–611 (2016).
17. Lundberg, E. & Borner, G. H. H. Spatial proteomics: a powerful discovery tool for cell biology. *Nat. Rev. Mol. Cell Biol.* **20**, 285–302 (2019).
18. Gatto, L. *et al.* A Foundation for Reliable Spatial Proteomics Data Analysis. *Mol Cell Proteomics* **13**, 1937–1952 (2014).
19. Andersen, J. S. *et al.* Proteomic characterization of the human centrosome by protein correlation profiling. *Nature* **426**, 570–574 (2003).
20. Foster, L. J. *et al.* A Mammalian Organelle Map by Protein Correlation Profiling. *Cell* **125**, 187–199 (2006).

21. Mulvey, C. M. *et al.* Using hyperLOPIT to perform high-resolution mapping of the spatial proteome. *Nat Protoc* **12**, 1110–1135 (2017).
22. Geladaki, A. *et al.* Combining LOPIT with differential ultracentrifugation for high-resolution spatial proteomics. *Nature Communications* **10**, 331 (2019).
23. Itzhak, D. N. *et al.* A Mass Spectrometry-Based Approach for Mapping Protein Subcellular Localization Reveals the Spatial Proteome of Mouse Primary Neurons. *Cell Reports* **20**, 2706–2718 (2017).
24. Jean Beltran, P. M., Mathias, R. A. & Cristea, I. M. A Portrait of the Human Organelle Proteome In Space and Time during Cytomegalovirus Infection. *cels* **3**, 361-373.e6 (2016).
25. Kennedy, M. A., Hofstadter, W. A. & Cristea, I. M. TRANSPIRE: A Computational Pipeline to Elucidate Intracellular Protein Movements from Spatial Proteomics Data Sets. *J. Am. Soc. Mass Spectrom.* **31**, 1422–1439 (2020).
26. Halliday, G. M. & Rana, S. Waveband and Dose Dependency of Sunlight-induced Immunomodulation and Cellular Changes†. *Photochemistry and Photobiology* **84**, 35–46 (2008).
27. Gatto, L., Breckels, L. M., Wieczorek, S., Burger, T. & Lilley, K. S. Mass-spectrometry-based spatial proteomics data analysis using pRoloc and pRolocdata. *Bioinformatics* **30**, 1322–1324 (2014).
28. Craxton, A. *et al.* PAXX and its paralogs synergistically direct DNA polymerase λ activity in DNA repair. *Nature Communications* **9**, 3877 (2018).
29. Brzoska, K. & Szumiel, I. Signalling loops and linear pathways: NF- B activation in response to genotoxic stress. *Mutagenesis* **24**, 1–8 (2008).
30. Remy, G. *et al.* Differential activation of p38MAPK isoforms by MKK6 and MKK3. *Cellular Signalling* **22**, 660–667 (2010).
31. Hintsala, H.-R., Siponen, M., Haapasaari, K.-M., Karihtala, P. & Soini, Y. Claudins 1, 2, 3, 4, 5 and 7 in solar keratosis and squamocellular carcinoma of the skin. *Int J Clin Exp Pathol* **6**, 2855–2863 (2013).
32. Hildesheim, J., Awwad, R. T. & Fornace, A. J. p38 Mitogen-Activated Protein Kinase Inhibitor Protects the Epidermis Against the Acute Damaging Effects of Ultraviolet Irradiation by Blocking Apoptosis and Inflammatory Responses. *Journal of Investigative Dermatology* **122**, 497–502 (2004).
33. Krenciute, G. *et al.* Nuclear BAG6-UBL4A-GET4 Complex Mediates DNA Damage Signaling and Cell Death. *J. Biol. Chem.* **288**, 20547–20557 (2013).
34. Nishi, R. *et al.* Centrin 2 Stimulates Nucleotide Excision Repair by Interacting with Xeroderma Pigmentosum Group C Protein. *Molecular and Cellular Biology* **25**, 5664–5674 (2005).
35. Trojan, P. *et al.* Light-dependent CK2-mediated phosphorylation of centrins regulates complex formation with visual G-protein. *Biochimica et Biophysica Acta (BBA) - Molecular Cell Research* **1783**, 1248–1260 (2008).
36. Franz, A. *et al.* Chromatin-associated degradation is defined by UBXN-3/FAF1 to safeguard DNA replication fork progression. *Nat Commun* **7**, (2016).
37. Verger, A. *et al.* Mechanisms Directing the Nuclear Localization of the CtBP Family Proteins. *Molecular and Cellular Biology* **26**, 4882–4894 (2006).
38. Wan, F. & Lenardo, M. J. The Nuclear Signaling of NF-κB – Current Knowledge, New Insights, and Future Perspectives. *Cell Res* **20**, 24–33 (2010).
39. Ito, S. *et al.* MMXD, a TFIIH-Independent XPD-MMS19 Protein Complex Involved in Chromosome Segregation. *Molecular Cell* **39**, 632–640 (2010).

40. Filhol, O. *et al.* Casein kinase II and the tumor suppressor protein P53 associate in a molecular complex that is negatively regulated upon P53 phosphorylation. *J. Biol. Chem.* **267**, 20577–20583 (1992).
41. Montenarh, M. Protein kinase CK2 in DNA damage and repair. *Translational Cancer Research* **5**, (2016).
42. Coin, F. *et al.* Phosphorylation of XPB helicase regulates TFIIH nucleotide excision repair activity. *The EMBO Journal* **23**, 4835–4846 (2004).
43. Grecu, D. & Assairi, L. CK2 phosphorylation of human centrins 1 and 2 regulates their binding to the DNA repair protein XPC, the centrosomal protein Sfi1 and the phototransduction protein transducin β. *FEBS Open Bio* **4**, 407–419 (2014).
44. Teitz, T. *et al.* Expression of the cDNA for the beta subunit of human casein kinase II confers partial UV resistance on xeroderma pigmentosum cells. *Mutation Research/DNA Repair* **236**, 85–97 (1990).
45. Cochet, C. & Chambaz, E. M. Oligomeric structure and catalytic activity of G type casein kinase. Isolation of the two subunits and renaturation experiments. *J Biol Chem* **258**, 1403–1406 (1983).
46. Delinasios, G. J., Karbaschi, M., Cooke, M. S. & Young, A. R. Vitamin E inhibits the UVAI induction of "light" and "dark" cyclobutane pyrimidine dimers, and oxidatively generated DNA damage, in keratinocytes. *Sci Rep* **8**, 1–12 (2018).
47. DJAVAHERI-MERGNY, M., GRAS, M.-P., MERGNY, J.-L. & DUBERTRET, L. UV-A-induced decrease in nuclear factor-κB activity in human keratinocytes. *Biochemical Journal* **338**, 607–613 (1999).
48. Saliou, C. *et al.* Antioxidants modulate acute solar ultraviolet radiation-induced NF-kappa-B activation in a human keratinocyte cell line. *Free Radical Biology and Medicine* **26**, 174–183 (1999).
49. Vile, G. F., Tanew-Ilitschew, A. & Tyrrell, R. M. Activation of NF-kappa B in human skin fibroblasts by the oxidative stress generated by UVA radiation. *Photochem Photobiol* **62**, 463–468 (1995).
50. Tebbe, B., Schwarz, C., Ruderisch, H. S., Treudler, R. & Orfanos, C. E. L-Ascorbic Acid Increases NFκB Binding Activity in UVA-Irradiated HaCaT Keratinocytes. *J Invest Dermatol* **117**, 154–156 (2001).
51. Yogev, O. *et al.* Fumarase: A Mitochondrial Metabolic Enzyme and a Cytosolic/Nuclear Component of the DNA Damage Response. *PLoS Biol* **8**, (2010).
52. Wang, G., Shang, L., Burgett, A. W. G., Harran, P. G. & Wang, X. Diazonamide toxins reveal an unexpected function for ornithine δ-amino transferase in mitotic cell division. *Proc Natl Acad Sci U S A* **104**, 2068–2073 (2007).
53. Sabouny, R. & Shutt, T. E. Reciprocal Regulation of Mitochondrial Fission and Fusion. *Trends in Biochemical Sciences* **45**, 564–577 (2020).
54. Twig, G. & Shirihai, O. S. The Interplay Between Mitochondrial Dynamics and Mitophagy. *Antioxid Redox Signal* **14**, 1939–1951 (2011).
55. Chatzidoukaki, O., Goulielmaki, E., Schumacher, B. & Garinis, G. A. DNA Damage Response and Metabolic Reprogramming in Health and Disease. *Trends in Genetics* **36**, 777–791 (2020).
56. Yefi, R. *et al.* Protein kinase CK2 promotes cancer cell viability via up-regulation of cyclooxygenase-2 expression and enhanced prostaglandin E2 production. *Journal of Cellular Biochemistry* **112**, 3167–3175 (2011).

57. Gray, G. K., McFarland, B. C., Rowse, A. L., Gibson, S. A. & Benveniste, E. N. Therapeutic CK2 inhibition attenuates diverse prosurvival signaling cascades and decreases cell viability in human breast cancer cells. *Oncotarget* **5**, 6484–6496 (2014).
58. Cooper, S. J. & Bowden, G. T. Ultraviolet B Regulation of Transcription Factor Families. *Curr Cancer Drug Targets* **7**, 325–334 (2007).
59. Djavaheri-Mergny, M. *et al.* UV-A irradiation induces a decrease in the mitochondrial respiratory activity of human NCTC 2544 keratinocytes. *Free Radical Research* **34**, 583–594 (2001).
60. Jugé, R. *et al.* Quantification and Characterization of UVB-Induced Mitochondrial Fragmentation in Normal Primary Human Keratinocytes. *Sci Rep* **6**, 35065 (2016).
61. Berneburg, M. *et al.* Induction of the Photoaging-Associated Mitochondrial Common Deletion In Vivo in Normal Human Skin. *J Invest Dermatol* **122**, 1277–1283 (2004).
62. Zhang, Z., Liu, L., Wu, S. & Xing, D. Drp1, Mff, Fis1, and MiD51 are coordinated to mediate mitochondrial fission during UV irradiation-induced apoptosis. *The FASEB Journal* **30**, 466–476 (2016).
63. Wang, P. *et al.* Dynamin-related protein Drp1 is required for Bax translocation to mitochondria in response to irradiation-induced apoptosis. *Oncotarget* **6**, 22598–22612 (2015).
64. Tondera, D. *et al.* SLP-2 is required for stress-induced mitochondrial hyperfusion. *The EMBO Journal* **28**, 1589–1600 (2009).
65. Willems, P. H. G. M., Rossignol, R., Dieteren, C. E. J., Murphy, M. P. & Koopman, W. J. H. Redox Homeostasis and Mitochondrial Dynamics. *Cell Metabolism* **22**, 207–218 (2015).
66. Rakovic, A. *et al.* Mutations in PINK1 and Parkin Impair Ubiquitination of Mitofusins in Human Fibroblasts. *PLOS ONE* **6**, e16746 (2011).
67. Rappsilber, J., Mann, M. & Ishihama, Y. Protocol for micro-purification, enrichment, pre-fractionation and storage of peptides for proteomics using StageTips. *Nat Protoc* **2**, 1896–1906 (2007).
68. Cox, J. & Mann, M. MaxQuant enables high peptide identification rates, individualized p.p.b.-range mass accuracies and proteome-wide protein quantification. *Nature Biotechnology* **26**, 1367–1372 (2008).
69. Cox, J. *et al.* Accurate Proteome-wide Label-free Quantification by Delayed Normalization and Maximal Peptide Ratio Extraction, Termed MaxLFQ *. *Molecular & Cellular Proteomics* **13**, 2513–2526 (2014).
70. Maaten, L. van der & Hinton, G. Visualizing Data using t-SNE. *Journal of Machine Learning Research* **9**, 2579–2605 (2008).
71. Rozenblatt-Rosen, O., Stubbington, M. J. T., Regev, A. & Teichmann, S. A. The Human Cell Atlas: from vision to reality. *Nature* **550**, 451–453 (2017).
72. The UniProt Consortium. UniProt: the universal protein knowledgebase. *Nucleic Acids Research* **45**, D158–D169 (2017).
73. Ashburner, M. *et al.* Gene Ontology: tool for the unification of biology. *Nature Genetics* **25**, 25–29 (2000).
74. Breckels, L. M., Mulvey, C. M., Lilley, K. S. & Gatto, L. A Bioconductor workflow for processing and analysing spatial proteomics data. *F1000Res* **5**, 2926 (2018).

Acknowledgments

We thank professor Marisa Helena Gennari de Medeiros for kindly providing access to her laboratory and equipment. We are grateful to professor Fabio Rodrigues and members of his laboratory, especially Evandro Pereira da Silva, for kindly helping with the solar simulator. We also thank Camille C. Caldeira da Silva and professor Alicia Kowaltowski for kindly helping with the Seahorse experiment. We are grateful to Dr. Mariana Pereira Massafera and MSc. Izaura Nobuko Toma for their technical assistance. The Redox Proteomics Core of the Mass Spectrometry Resource at Chemistry Institute, University of Sao Paulo, is acknowledged for access to state-of-the-art MS instrumentation. The Albert Einstein Hospital is also acknowledged for technical assistance and access to the confocal microscope.

Funding

Fundação de Amparo à Pesquisa do Estado de São Paulo (FAPESP) grant 2012/12663-1 (PDM)
FAPESP grant 2016/11430-4 (HPV)
FAPESP grant 2016/00696-3 (GER)
FAPESP grant 15/07768-7 (FGR)
CEPID Redoxoma grant 2013/07937-8 (PDM)
Conselho Nacional de Desenvolvimento Científico e Tecnológico grant 402683/2016-1 (GER)
Conselho Nacional de Desenvolvimento Científico e Tecnológico grant 302120/2018-1 (PDM)
NAP Redoxoma PRPUSP 2011.1.9352.1.8 (PDM)
John Simon Guggenheim Memorial Foundation (PDM)

Authors Contribution

HPV, GER and PDM conceptualized the study. HPV performed experiments, analyzed the data and wrote the first draft of the manuscript. FGR and APYC performed the immunofluorescence assays and discussed the results. BDCC performed the comet assay experiment and also discussed the results. GER and PDM acquired funding, provided the resources, critically read and edited the final version of the manuscript.

Competing interests

The authors declare no competing interests.

Data availability

The proteomic dataset generated during this study has been deposited to the ProteomeXchange Consortium (http://www.proteomexchange.org/) via the PRIDE repository (identifier: PXD027941). All processed data are available in the Supporting Information.

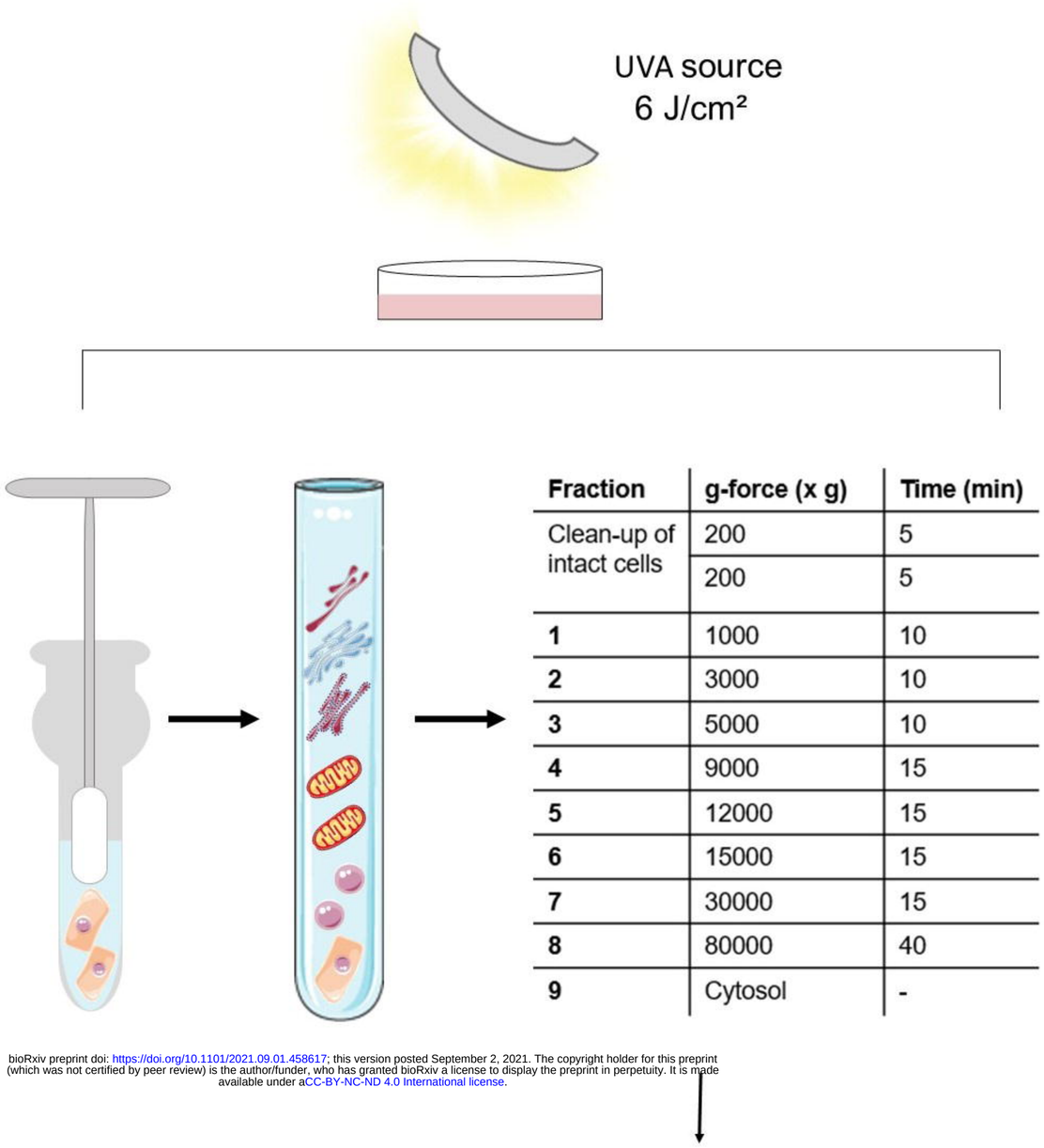

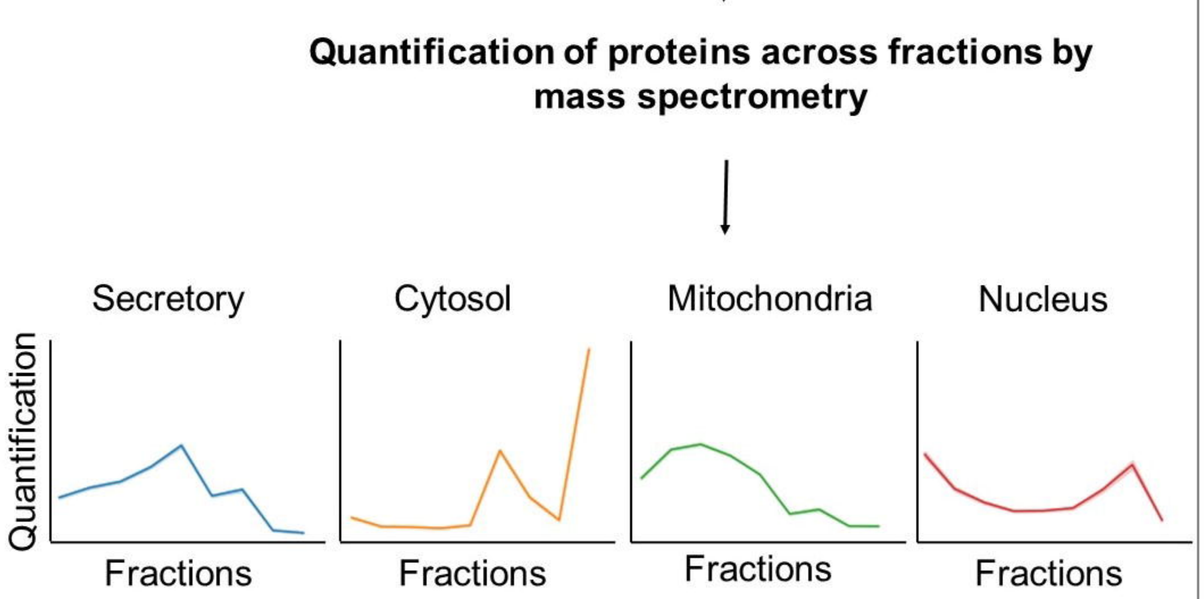

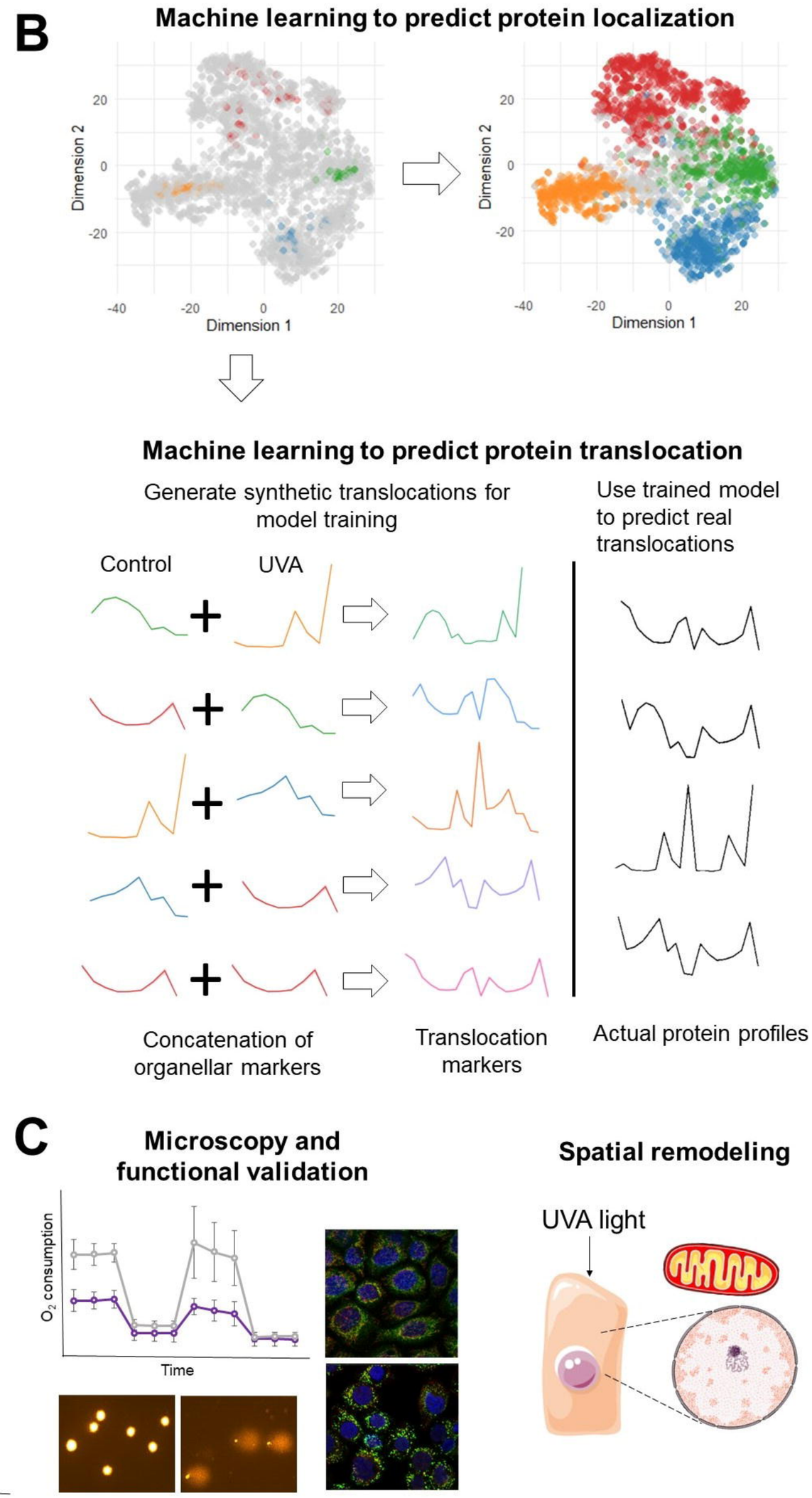

Fig. 1. Proteomic approach to define spatial changes in protein distribution upon light stress.

(A) Experimental protocol. **(B)** Computational pipelines used to define changes in subcellular organization promoted by UVA light in HaCaT cells. **(C)** Validation of results using traditional biochemical assays.

Fig. 2. Identification of subcellular patterns in HaCaT's spatial proteomics dataset.

(A) Profile plots of organellar markers in the HaCaT dataset. Shadowed intervals represent standard errors, and values represent means. Five biological replicates per group were employed for the spatial proteomics experiment.
(B) 3D representation of subcellular fractionation data using t-SNE. The maps were overlaid with organellar markers.
(C) t-SNE plots of all control and irradiated samples overlaid with the most frequent classifications obtained for each protein across replicates using the neural network algorithm for predicting localization. **(D)** Numbers of proteins assigned to the cytosol, mitochondria nucleus and secretory organelles by condition. Bars represent the mean number of proteins assigned to each compartment, and error bars represent the standard deviation. **(E)** Reproducibility of classifications across replicates. Bars represent the percentage of proteins that received the same classification in 3, 4 or 5 biological replicates out of the total 5. **(F)** Accuracy of the neural network predictions obtained by comparing the predicted subcellular localizations with Gene Ontology information. Bars represent means per condition, and error bars represent standard deviations. **(G)** t-SNE plots overlaid with sub-organellar markers and colocalizing protein complexes.

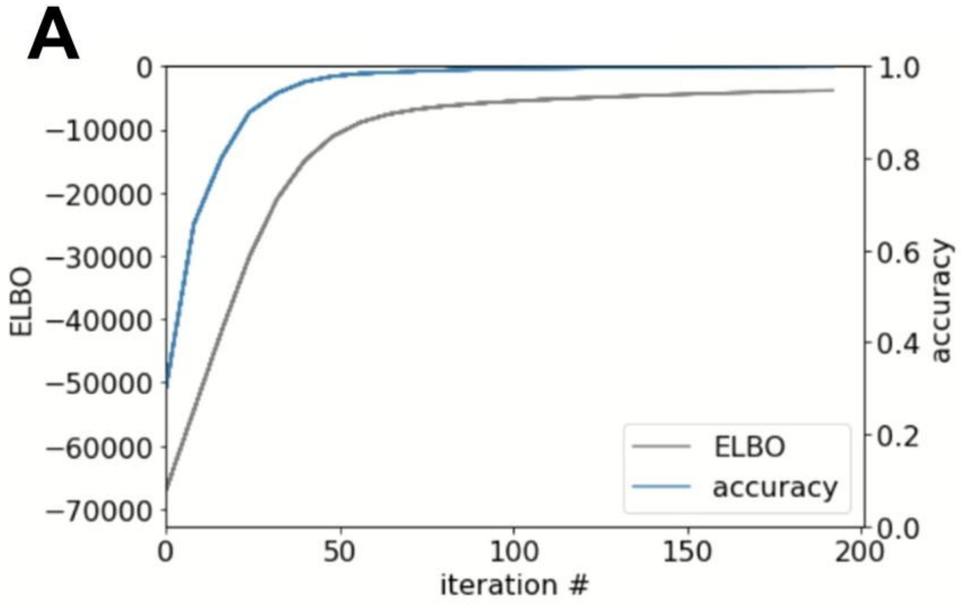

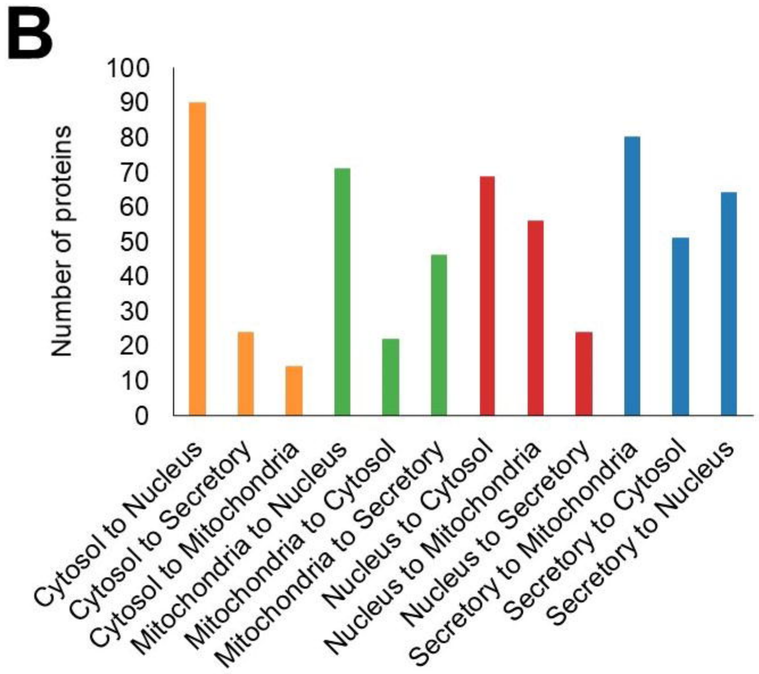

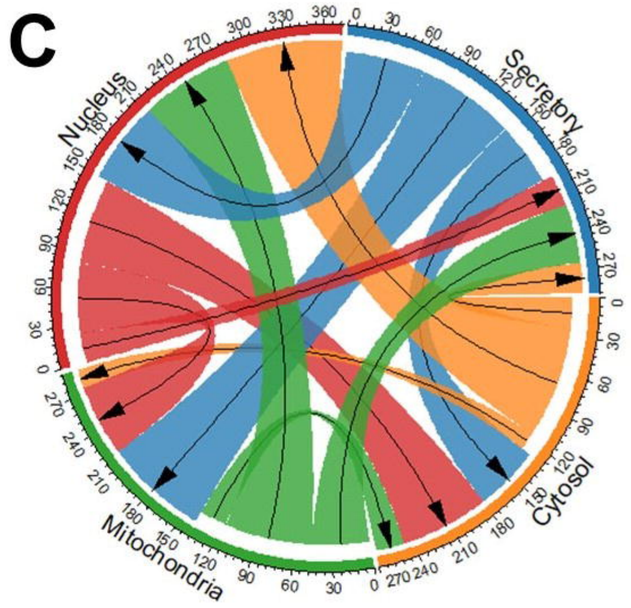

D

GO: Biological Process	Adj. p-value
Intracellular protein transport	4.89×10^{-11}
Mitochondrial translation termination	7.61×10^{-11}
Mitochondrial translational elongation	9.16×10^{-13}
Cellular protein localization	3.64×10^{-8}
Organelle organization	1.47×10^{-8}

GO: Cellular Compartment	Adj. p-value
Mitochondrial matrix	2.02×10^{-15}
Mitochondrial membrane	9.19×10^{-14}
Mitochondrial inner membrane	1.45×10^{-13}
Organelle inner membrane	3.74×10^{-12}
Intracellular organelle lumen	1.22×10^{-10}

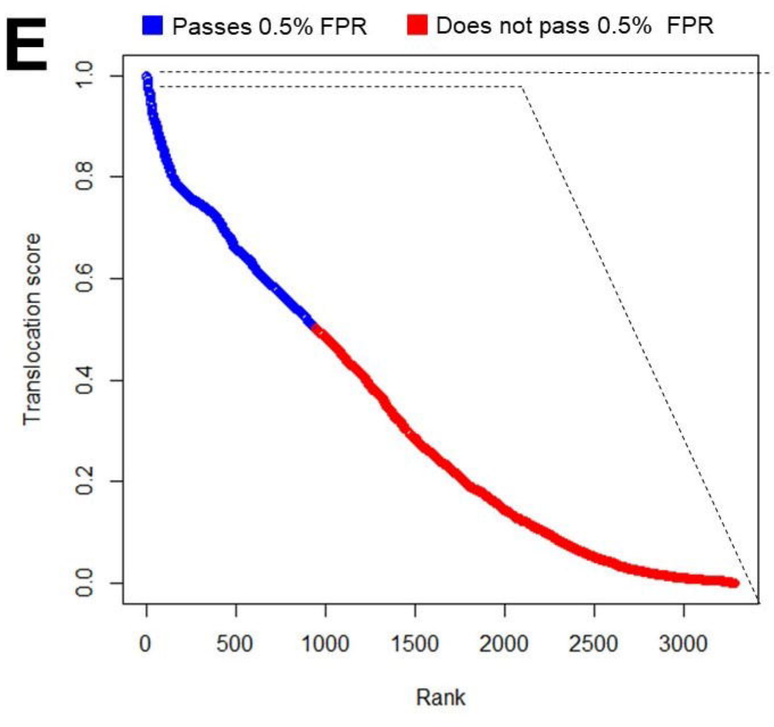

TOP 12	
MAP2K3	Dual specificity mitogen-activated protein kinase kinase 3
ATL2	Atlastin-2
CLDN7	Claudin-7
PARP4	Protein mono-ADP-ribosyltransferase PARP4
OAS1	Serine/threonine-protein kinase OSR1
YTHDF2	YTH domain-containing family protein 2
PIGK	GPI-anchor transamidase
RPS6KA4	Ribosomal protein S6 kinase alpha-4
DPYSL3	Dihydropyrimidinase-related protein 3
P4HA1	Prolyl 4-hydroxylase subunit alpha-1
RNF114	E3 ubiquitin-protein ligase RNF114
APOL2	Apolipoprotein L2

Fig. 3. Prediction of UVA-induced translocations in HaCaT cells.

(A) Accuracy and Evidence Lower Bounds (ELBO) obtained for the classifier during training. **(B)** Number of proteins of each translocation class assigned by the algorithm. **(C)** Circular plot representing UVA-induced translocations between subcellular niches as identified by the classifier. **(D)** Enrichment analysis of the translocation targets based on Gene Ontology terms. **(E)** Rank order plot of the translocation scores obtained for each protein by the machine learning modeling. The top 12 highest scoring proteins are highlighted in a table to the right of the rank order plot.

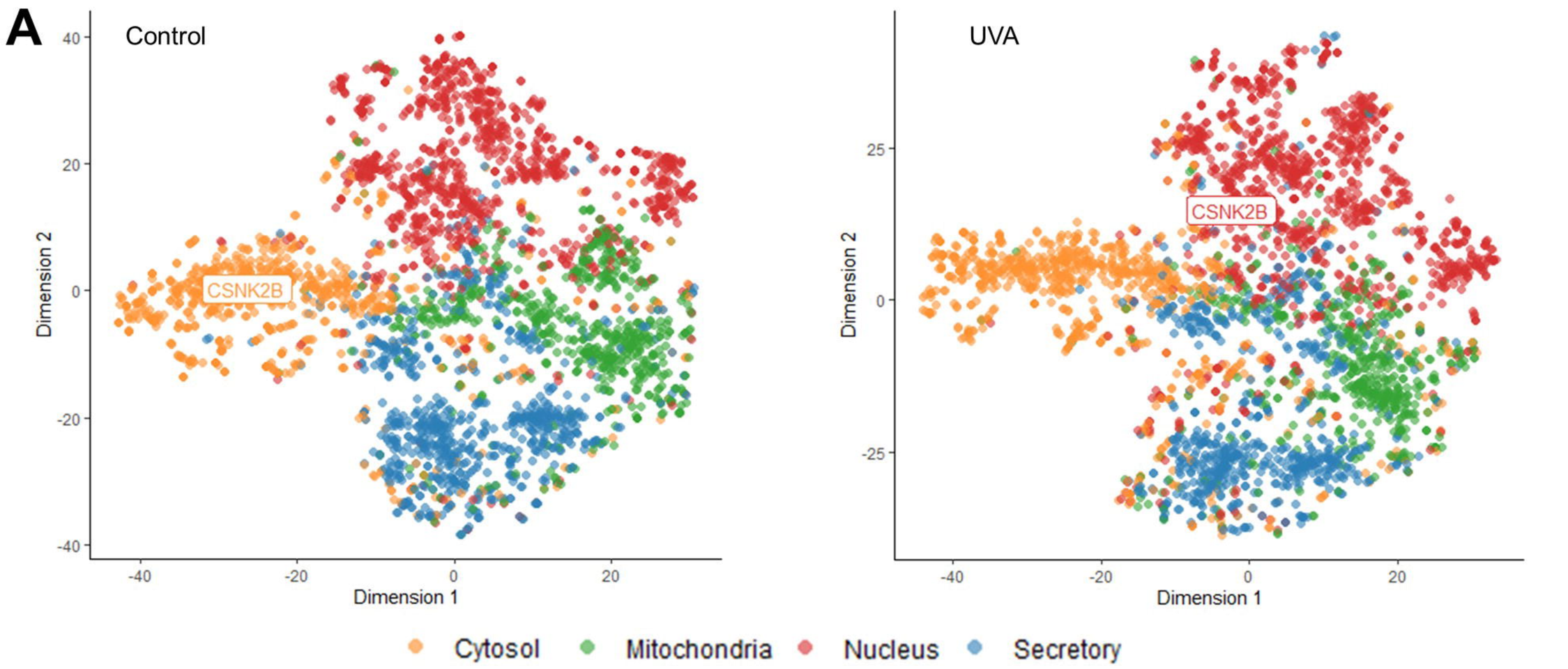

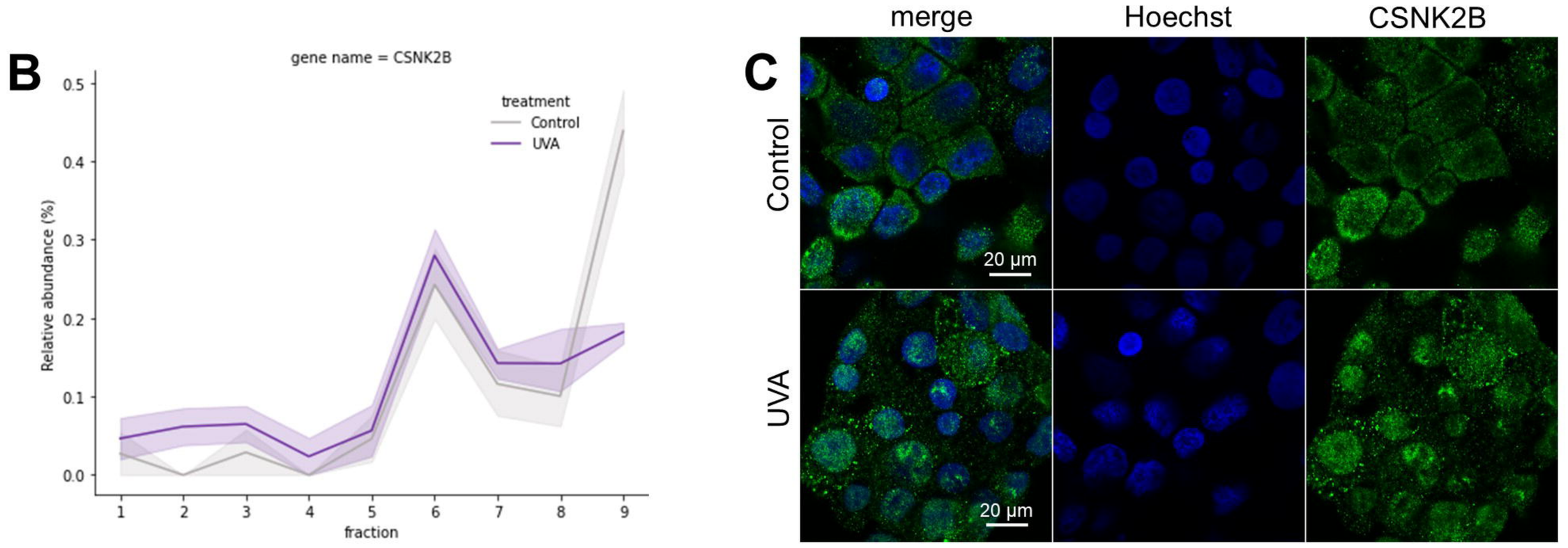

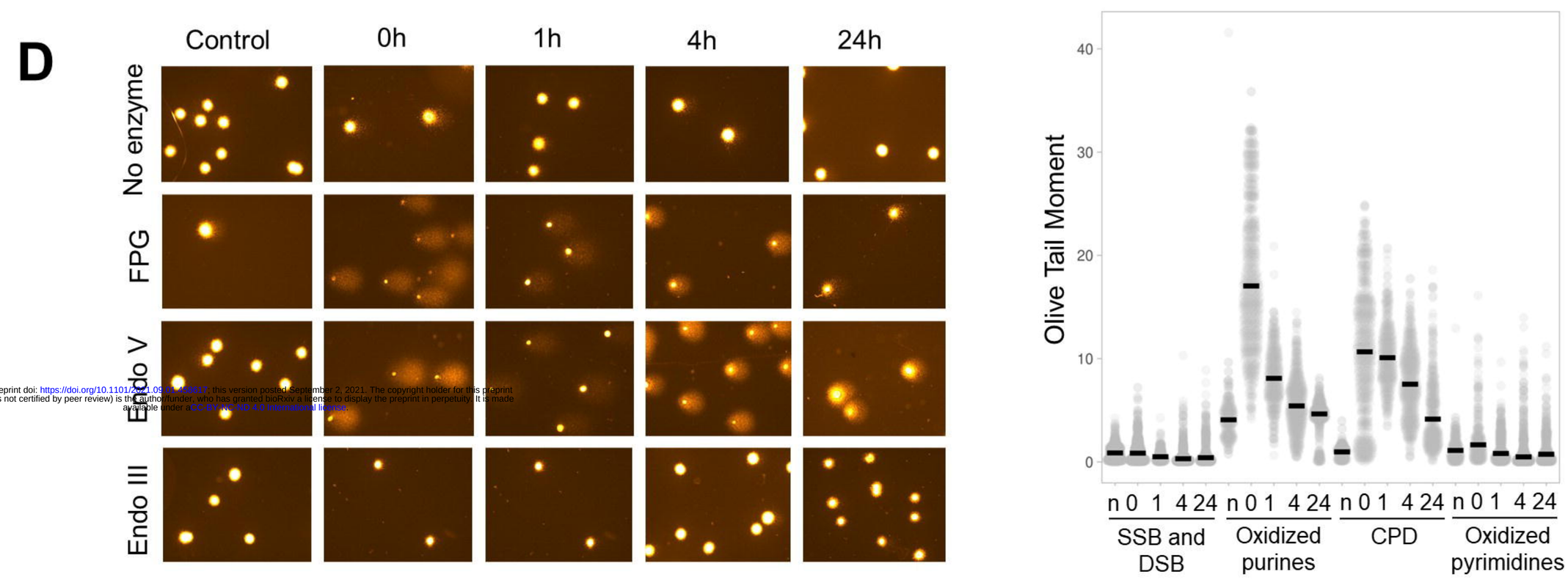

Fig. 4. CSNK2B translocates to the nucleus upon DNA damage induced by UVA exposure.

(A) 2D t-SNE plots representing the migration of CSNK2B from the cytosolic cluster in control samples to the nuclear cluster in UVA-irradiated cells. Colors represent the translocations predicted by the classifier (organelle of origin in controls and destination in UVA plot). **(B)** Profile plot obtained for CSKN2B in controls and irradiated samples. Lines represent the means of relative abundance, and shadowed intervals represent the standard errors. **(C)** Representative immunofluorescence images showing CSNK2B translocation from the cytosol to the nucleus after exposing HaCaT cells to UVA light. CSNK2B was immunostained (green), and the nucleus was stained with Hoechst (blue). Three independent replicates per group were analyzed. **(D)** Comet assay results for control and irradiated cells. Representative images of randomly scored comets in slides from all conditions are represented on the left. The graph shows the semi-quantification of each type of DNA damage over time. Points represent Olive Tail Moments scored for all measured cells, and black bars represent the medians of all points (n = 4 independent experiments).

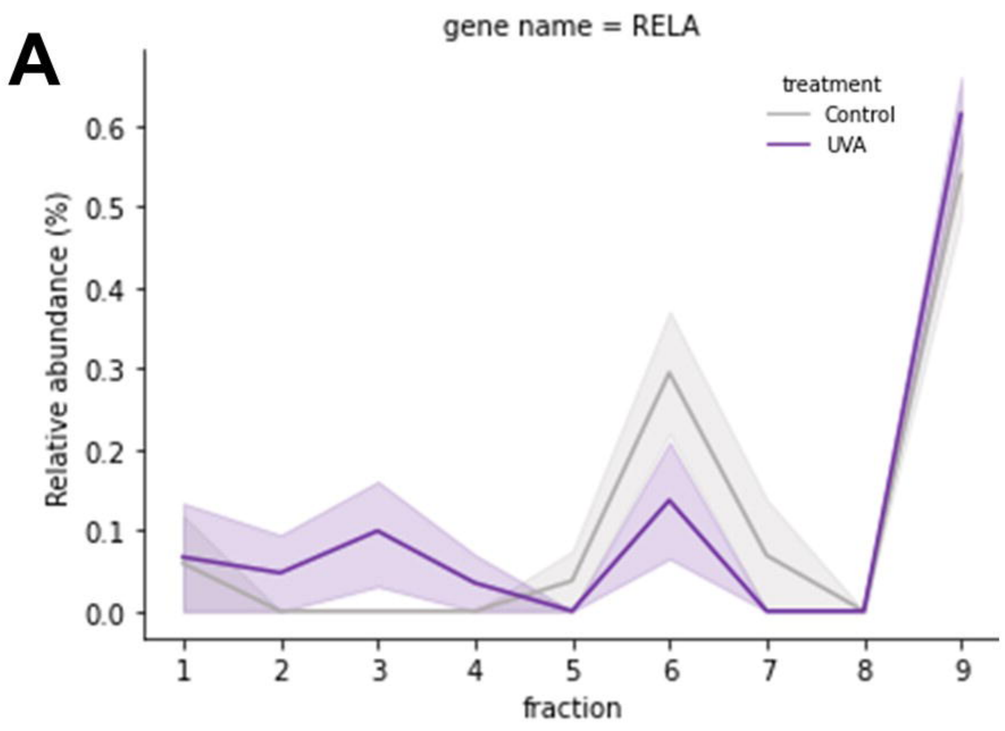

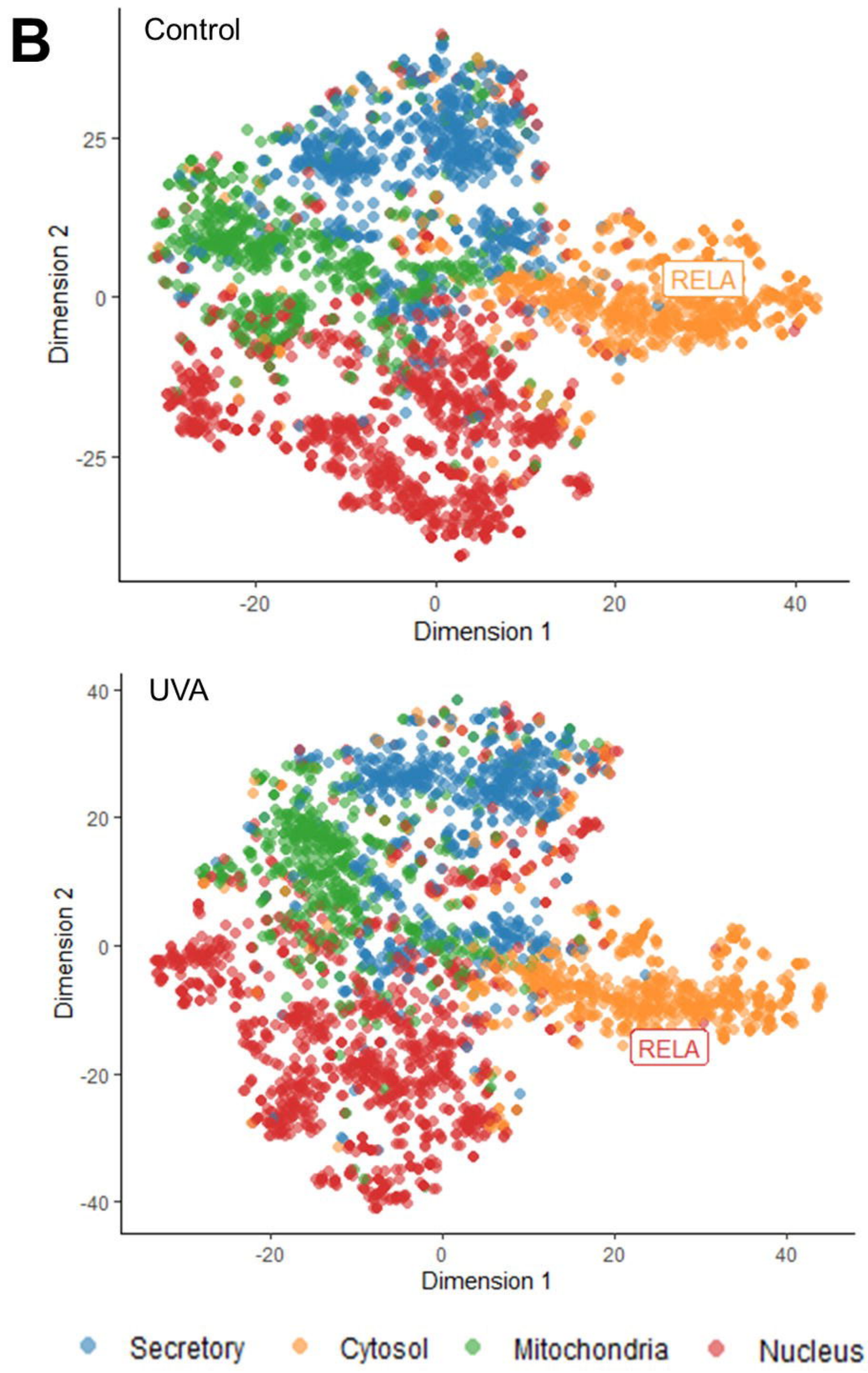

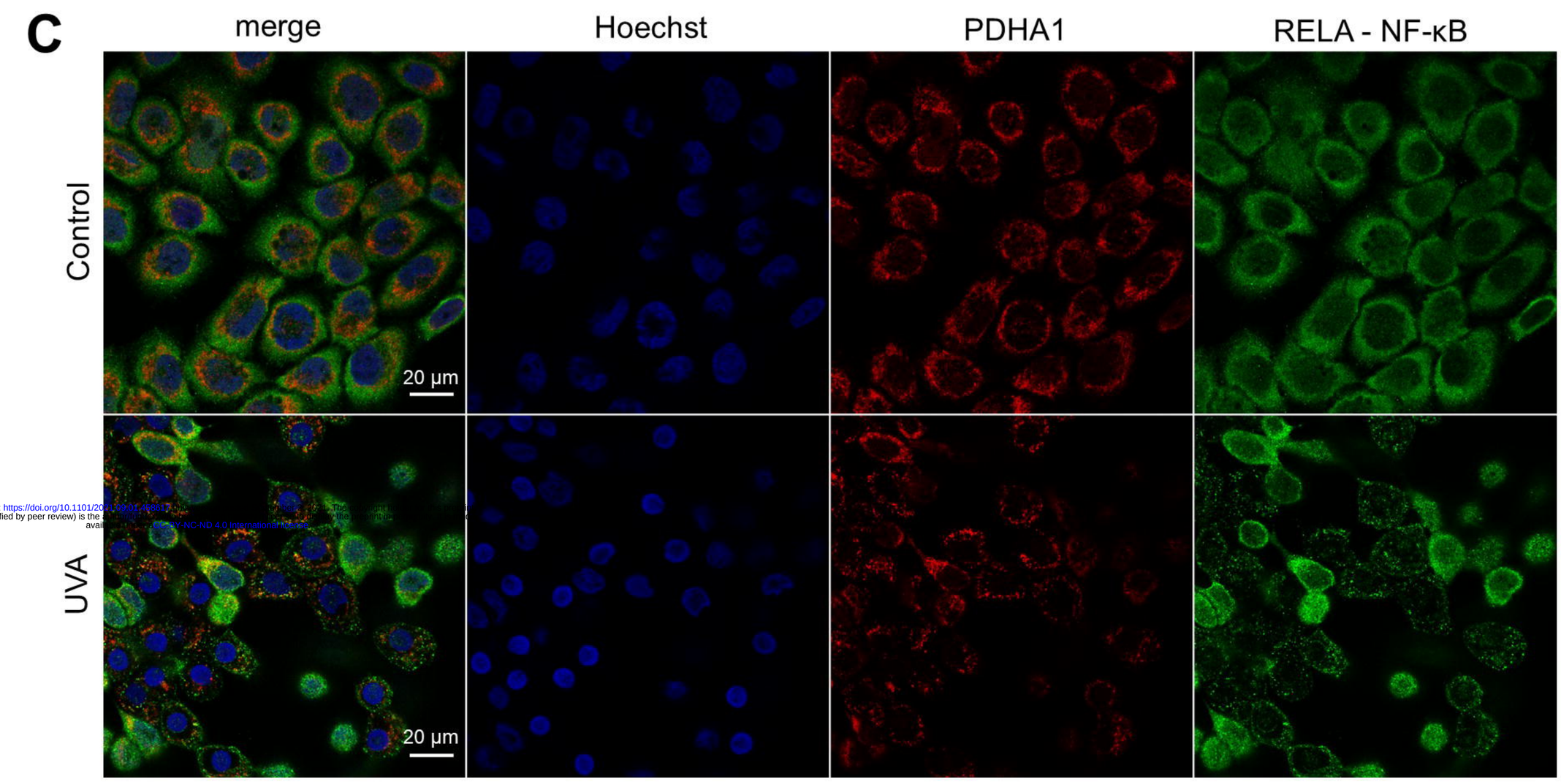

Fig. 5. UVA light induces NF-κB RELA subunit degradation.

(A) Profile plots obtained for RELA in controls and irradiated samples. Lines represent the means of relative abundance, and shadowed intervals represent the standard errors. **(B)** 2D t-SNE plots representing the migration of RELA from the cytosolic cluster in control samples to the interface between the cytosolic and nuclear clusters in UVA-irradiated cells. Colors represent the translocations predicted by the classifier (organelle of origin in controls and destination in UVA plot). **(C)** Immunostaining of NF-κB RELA subunit (green) in control and UVA-irradiated samples. The nucleus was stained with Hoechst (blue). Mitochondria were stained by immunolabeling of pyruvate dehydrogenase (PDHA1, red). n = 3 independent biological replicates.

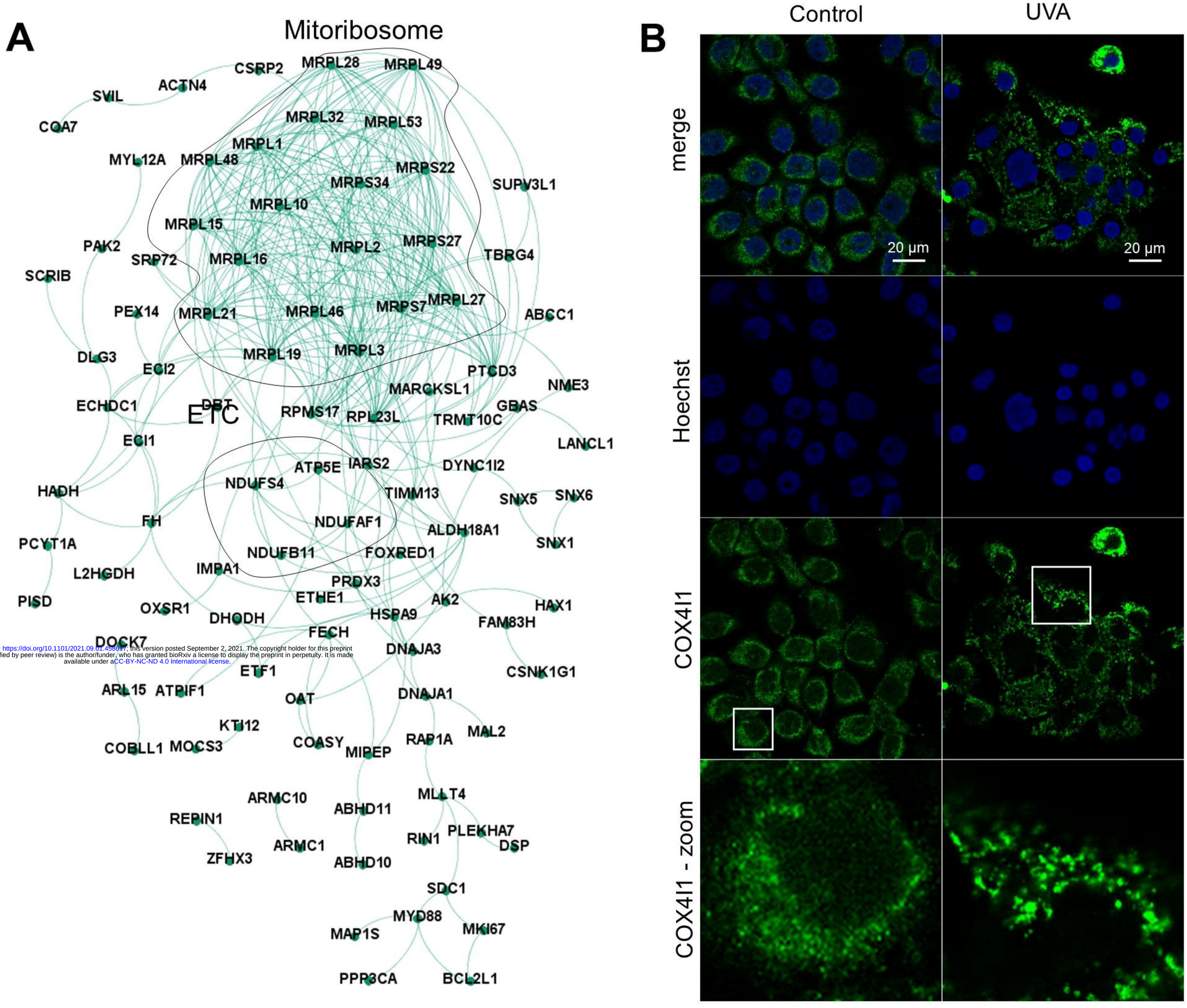

Fig. 6. UVA induces changes in mitochondrial morphology that are associated with changes in protein fractionation.

(A) String network of proteins that the learning classifier identified as translocating from the mitochondria to other compartments in response to UVA. Nodes represent proteins, and the edges represent physical interactions between proteins. **(B)** Immunostaining of COX4I1 (green). The nucleus was stained with Hoechst (blue). Two biologically independent experiments were performed, with similar results obtained.

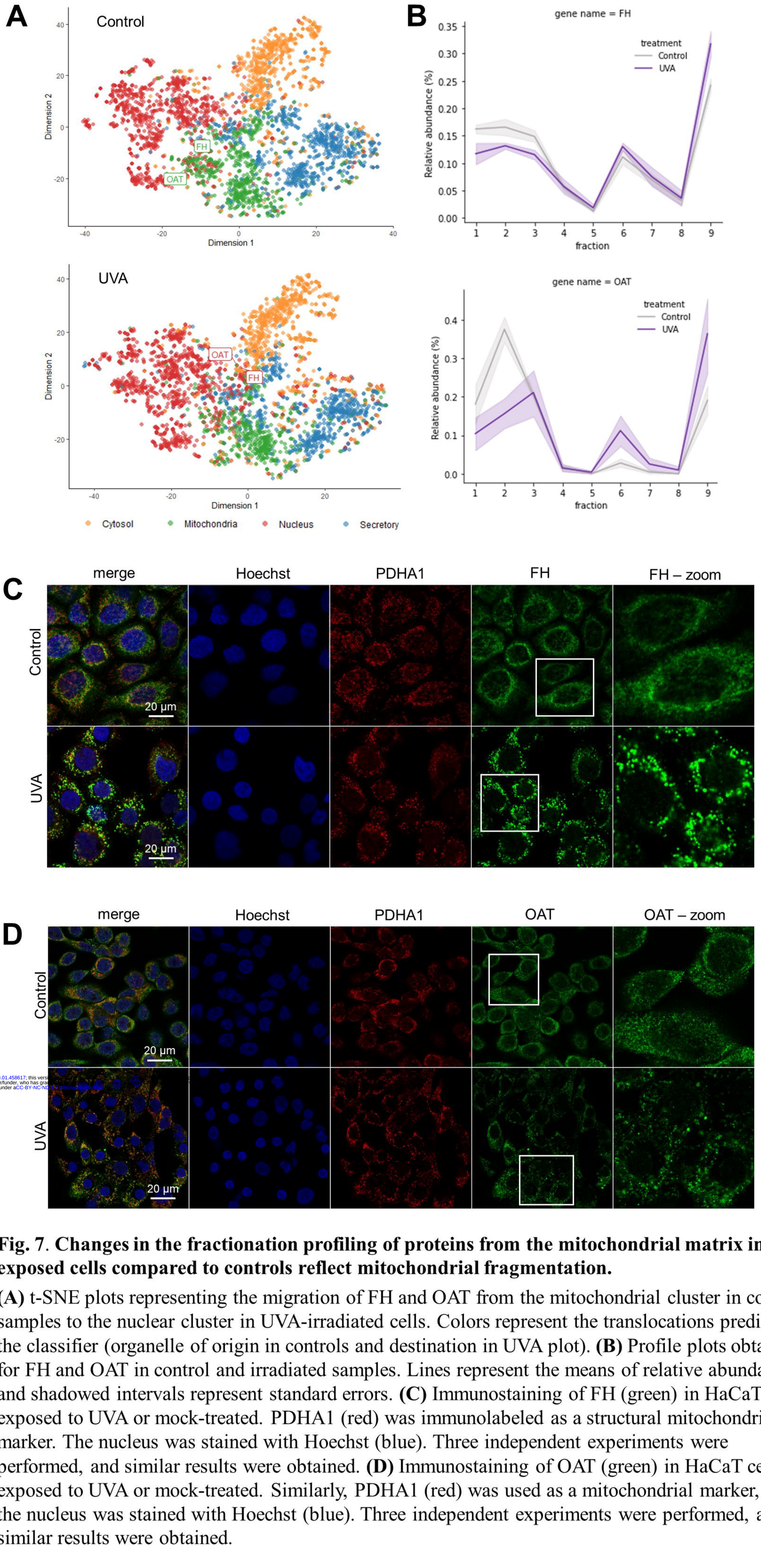

Fig. 7. Changes in the fractionation profiling of proteins from the mitochondrial matrix in UVA-exposed cells compared to controls reflect mitochondrial fragmentation.

(A) t-SNE plots representing the migration of FH and OAT from the mitochondrial cluster in control samples to the nuclear cluster in UVA-irradiated cells. Colors represent the translocations predicted by the classifier (organelle of origin in controls and destination in UVA plot). **(B)** Profile plots obtained for FH and OAT in control and irradiated samples. Lines represent the means of relative abundance, and shadowed intervals represent standard errors. **(C)** Immunostaining of FH (green) in HaCaT cells exposed to UVA or mock-treated. PDHA1 (red) was immunolabeled as a structural mitochondrial marker. The nucleus was stained with Hoechst (blue). Three independent experiments were performed, and similar results were obtained. **(D)** Immunostaining of OAT (green) in HaCaT cells exposed to UVA or mock-treated. Similarly, PDHA1 (red) was used as a mitochondrial marker, and the nucleus was stained with Hoechst (blue). Three independent experiments were performed, and similar results were obtained.

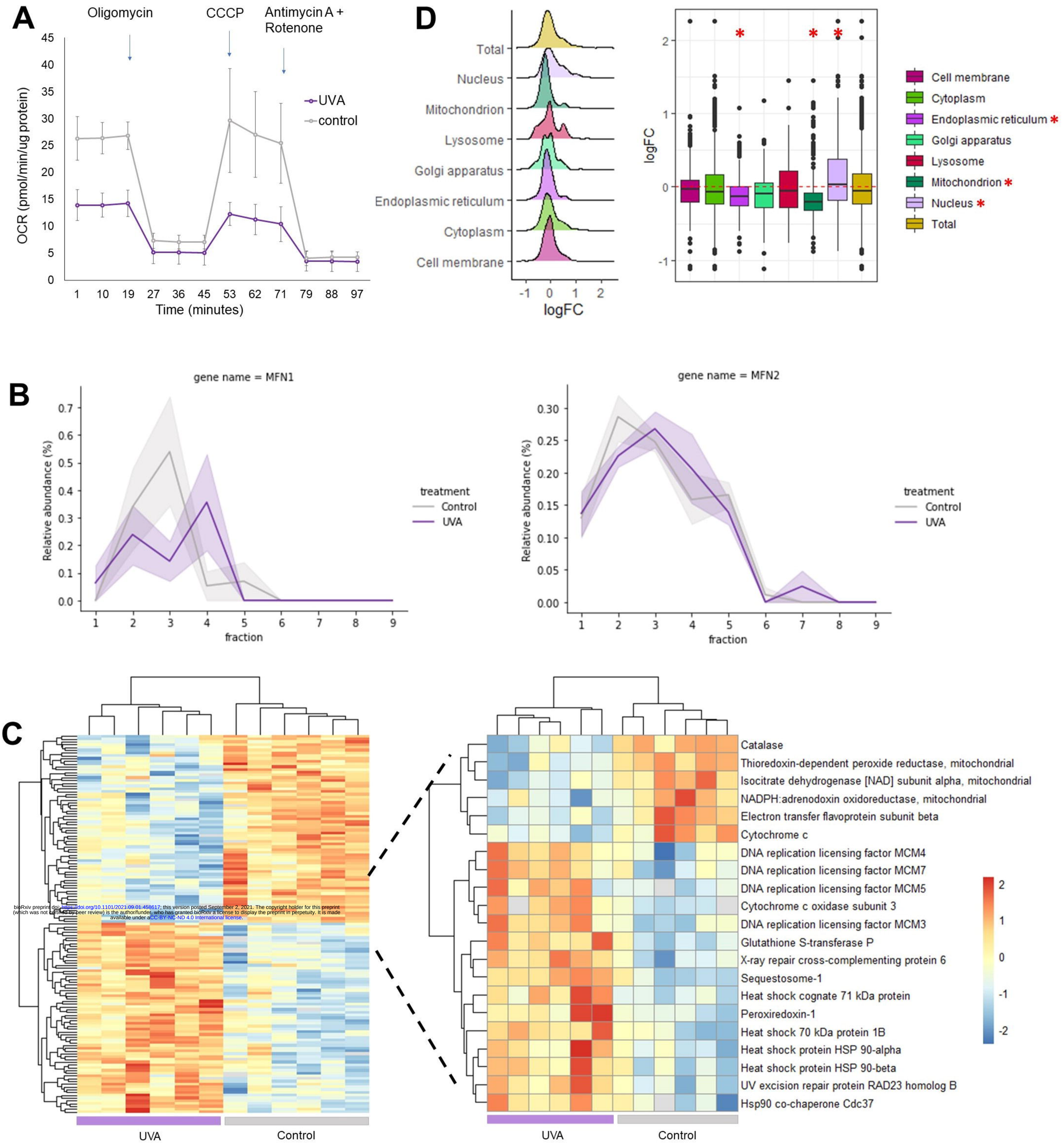

Fig. 8: UVA-induced changes in mitochondrial dynamics impact respiratory function.

(A) Oxygen consumption rates (OCR) were measured in irradiated and control cells before and after the addition of 1 µM oligomycin, 1 µM CCCP and a solution containing 1 µM antimycin and 1 µM rotenone (n = 4). **(B)** Profile plots of MFN1 and MFN2. Lines represent the means of relative abundance, and shadowed intervals represent the standard errors. **(C)** Hierarchical clustering of differentially regulated proteins comparing HaCaT cells exposed to UVA versus controls (Student's T-test, 0.05 FDR correction). The color gradient represents z-scored LFQ intensities, and columns represent replicates (n = 6 per group). Stress-responsive proteins are highlighted. **(D)** Compartment-specific proteome changes in irradiated versus control HaCaT cells one and a half hours after UVA exposure (n = 6). Values are expressed in $\log_2$ (Fold Change UVA/control).